

# Dominance of Magnetic Cataclysmic Variables in the Resolved Galactic Ridge X-ray Emission of the Limiting Window

JaeSub Hong<sup>1\*</sup>

<sup>1</sup>*Harvard-Smithsonian Center for Astrophysics, 60 Garden St., Cambridge, MA 02138*

26 February 2024

## ABSTRACT

The diffuse appearance of the Galactic Ridge X-ray Emission (GRXE) has been puzzling since its discovery due to lack of compelling theories for sustainable hot diffuse X-ray emission in the Galactic plane. Recently [Revnivtsev et al. \(2009\)](#) (R09) claimed that  $\sim 90\%$  of the 6.5–7.1 keV X-ray flux from a small section of a low extinction region at  $1.4^\circ$  south of the Galactic Center has been resolved to discrete sources with  $L_{X, 2-10 \text{ keV}} \gtrsim 4 \times 10^{-16} \text{ erg s}^{-1} \text{ cm}^{-2}$ , using ultra-deep (1 Ms) *Chandra* ACIS-I observations. They also concluded that coronally active stars such as active binaries (ABs) contribute  $\sim 60\%$  of the resolved flux. However, our recent discovery of a large population of magnetic cataclysmic variables (MCVs) in the same region suggests their significant role in the resolved hard X-ray flux. In addition, deep X-ray surveys of other several Galactic Bulge fields over the past decade have indicated that MCVs are likely the major contributor in the hard X-ray emission above 2–3 keV. To solve this mystery, we have conducted an independent indepth analysis of discrete X-ray sources in the low extinction region. The total fraction of the 6.5–7.1 keV flux we can confidently claim as resolved is  $\sim 70\text{--}80\%$ , which largely agrees with R09 but leaves some room for diffuse components. However, despite the various attempts, we consistently find that the resolved hard X-ray flux above 3 keV is dominated by relatively bright, hard X-ray sources such as MCVs, whereas the contribution from relatively faint, soft sources such as ABs is below 20%. We describe in detail our analysis procedure in order to elucidate possible origins of the discrepancy.

**Key words:** Galaxy: bulge — X-ray: binaries — cataclysmic variables

## 1 INTRODUCTION

The X-ray glows along the Galactic plane, discovered almost 30 years ago, form a narrow continuous X-ray bright ridge, known as the Galactic Ridge X-ray Emission (GRXE) ([Worrall et al. 1982](#); [Warwick et al. 1985](#); [Koyama et al. 1986](#)). The origin of the GRXE, whether truly diffuse or from unresolved discrete sources, has been debated ever since. The GRXE resembles X-ray emission from an optically thin plasma of a high temperature (a few keV) with emission lines from highly ionized heavy elements such as Si and Fe ([Koyama et al. 1986](#); [Yamauchi & Koyama 1993](#)). However, the shallow Galactic gravity and lack of energy source to sustain such a plasma suggest discrete sources as the origin

of the GRXE ([Worrall & Marshall 1983](#); [Yamauchi et al. 1996](#); [Kaneda et al. 1997](#)).

With subarcsec angular resolution and superb sensitivity, the *Chandra* X-ray Observatory launched a decade ago brought a new hope of revealing the nature of the GRXE. The early studies by [Ebisawa et al. \(2001, 2005\)](#) using deep *Chandra* observations (100 ks each) of two adjacent Galactic plane fields at  $(l, b) = (28.5^\circ, -0.2^\circ)$  showed the GRXE in the 2–10 keV band is largely unresolved with discrete sources of  $L_{X, 2-10 \text{ keV}} \gtrsim 3 \times 10^{-15} \text{ erg s}^{-1} \text{ cm}^{-2}$ . They claimed the unresolved X-ray flux cannot be explained by the known types of undetected, fainter discrete X-ray sources, suggesting a significant portion of the GRXE is truly diffuse. However, [Revnivtsev & Sazonov \(2007\)](#) claimed the GRXE in the same region can be explained by discrete sources when taking into account a large number of unresolved, faint, coronally active X-ray sources such as active binaries (ABs).

\* E-mail: [jaesub@head.cfa.harvard.edu](mailto:jaesub@head.cfa.harvard.edu)

**Table 1.** *Chandra* ACIS-I observations of the LW

Obs. ID	Start Time (UT: y/m/d h:m)	R.A. ( $^{\circ}$ )	Decl. ( $^{\circ}$ )	Offset <sup>a</sup> ( $'$ )	Roll ( $^{\circ}$ )	Exposure (ks)	GTI <sup>b</sup> (ks)	Obs. Mode	Chips
6362	2005/08/19 16:15	267.86694	-29.59235	0.1	273	38	37.7	<i>F</i>	0123..67..
5934	2005/08/22 08:16	267.86692	-29.59233	0.1	273	41	30.8	<i>F</i>	0123..67..
6365	2005/10/25 14:55	267.86630	-29.59212	0.1	265	21	20.7	<i>F</i>	0123..67..
9505	2008/05/07 15:29	267.85740	-29.57123	1.3	82	11	10.7	<i>VF</i>	0123..6...
9855	2008/05/08 05:00	267.85741	-29.57124	1.3	82	57	55.9	<i>VF</i>	0123..6...
9502	2008/07/17 15:45	267.86685	-29.59108	-	281	167	164.1	<i>VF</i>	0123..6...
9500	2008/07/20 08:11	267.86148	-29.58793	0.3	280	165	162.6	<i>VF</i>	0123..6...
9501	2008/07/23 08:13	267.86399	-29.58953	0.2	279	135	131.0	<i>VF</i>	0123..6...
9854	2008/07/27 05:53	267.87404	-29.59630	0.5	278	25	22.8	<i>VF</i>	0123..6...
9503	2008/07/28 17:37	267.86852	-29.59311	0.2	275	103	102.3	<i>VF</i>	0123..6...
9892	2008/07/31 08:07	267.86853	-29.59312	0.2	275	65	65.8	<i>VF</i>	0123..6...
9893	2008/08/01 02:44	267.87098	-29.59490	0.3	275	45	42.2	<i>VF</i>	0123..6...
9504	2008/08/02 21:23	267.87097	-29.59490	0.3	275	127	125.4	<i>VF</i>	0123..6...

Notes. <sup>a</sup>The aim point offset relative to Obs. ID 9502. Table 1 in H12 shows the target coordinates of each pointing. <sup>b</sup>The Good Time Intervals (GTIs) are selected by the fluctuations ( $< 3\sigma$ ) of the background event rates in the 2.5–7 keV band, which is calculated after the discrete source contribution is removed. The GTIs shown here are based on the events processed through the EDSEER routine and the *VF* mode cleaning (see §3.1). An additional manual inspection ensures the removal of the background flaring periods. As a result, the selected GTIs are slightly different from those in Table 1 in H12 (see the text).

Motivated by the resemblance of the Galactic distribution of the GRXE and the near infrared (nIR) emission measured by Spitzer that closely follows stellar population (Revnivtsev et al 2006), Revnivtsev et al. (2009, hereafter R09) conducted ultra-deep observations (1 Ms) of a low extinction region (Limiting Window; LW)<sup>1</sup> at  $1.4^{\circ}$  south of the Galactic Center. They claimed that  $88 \pm 12\%$  of the highly ionized iron emission line (6.5–7.1 keV) in the GRXE is resolved to discrete sources and the known contribution of the Cosmic X-ray Background (CXB). Again they claimed a large fraction ( $\sim 60\%$ ) of the resolved flux is from relatively faint, soft coronal X-ray sources such as ABs.

Meanwhile, several surveys have been conducted to study faint X-ray sources in the Galactic plane and Bulge fields in order to understand their composition, which can lead to clues of formation and evolutionary history of X-ray sources as well as Galactic Bulge and Galaxy (e.g. Munro et al. 2003, 2009; Hong et al. 2009b, hereafter M03, M09, H09b). The studies of newly discovered several thousands of Bulge X-ray sources in these fields have indicated that the hard X-ray emission is dominated by low luminosity ( $L_X \lesssim 10^{32-33}$  erg s $^{-1}$ ) hard X-ray sources and that their major candidates are likely magnetic cataclysmic variables (MCVs) (Laycock et al. 2005, M09, H09b).

The LW is one of the low extinction Bulge fields, and the first deep *Chandra* (100 ks) exposure of the region was conducted as a part of our survey to understand the population of Galactic Bulge X-ray sources (H09b, van den Berg et al. 2006; van den Berg, Hong & Grindlay 2009, hereafter V09). Our recent discovery of periodic sources in the LW also indicates a large population of MCVs in the region and their significant role in the resolved hard X-ray flux (Hong et al. 2012a, hereafter H12). A recent spectral analysis of the GRXE using the *Suzaku* observations also shows the dominance of the MCVs in the hard X-ray band of the GRXE (Yuasa, Makishima & Nakazawa 2012, see also Morihana et al. 2012).

Motivated by this new puzzle in source composition of

the resolved GRXE and their contribution in the hard X-ray flux, we have conducted an independent indepth analysis of X-ray sources found in the combined ultra-deep *Chandra* exposure of the LW. In particular, the advanced source search routine employed by R09 seems to nearly double the source number compared to other conventional methods (§§3.3 & 4.1). Despite the differences among the source search routines, the lack of studies comparing the results in the past also motivates us to conduct this comparative study of the source search routines for future analysis of other fields. We summarize the observations (§2) and describe in detail our analysis procedure (§3). We present our results in comparison with R09 (§4): the possible origins of the discrepancy are presented in the Appendix. We also discuss the implications of our findings for future studies (§5).

## 2 OBSERVATIONS

The LW was observed for a total of 1 Ms exposure (100 ks in 2005 and 900 ks in 2008) with the *Chandra* ACIS-I instrument. Table 1 shows the basic observational parameters (see also R09 and Table 1 in H12). The observations in 2005 were conducted in *Faint* mode (*F* mode) with 6 ACIS CCDs enabled, and the rest in *Very Faint* mode (*VF* mode) with 5 ACIS CCDs enabled. The *VF* mode allows an additional background reduction (see §3.1) (Vikhlinin 2002). The CCD readout time and thus the correction factor for the readout background depend on the number of enabled CCDs (e.g. 41 ms readout time with 3.2s frame time for 6 CCDs) (Markvitch et al. 2000). The aim points of the observations varied about  $0.1'$  to  $1.3'$  from each other. The roll angles of two observations ( $\sim 70$  ks) in 2008 were about  $200^{\circ}$  off from the rest. The roll angle and aim point variations made the CCD gaps less prominent in the merged data set.

## 3 DATA ANALYSIS

The analysis procedures for discrete sources can be grouped into four main steps: event processing & selection, stacking,

<sup>1</sup> R09 call this region the  $1.5^{\circ}$  Window.

**Table 2.** Key Parameters of Various Analysis Approaches (the Default Options in Bold)

Analysis Stages	Parameters	Options Tested & Results Quoted in This Paper (Bold)
Event Process (§3.1)	Pixel Repositioning; VF Mode Cleaning	1) <b>EDSER; Yes</b> 2) EDSER; No 3) Random; No* 4) None; Yes
Event Merge (§3.2)	Boresight Correction; Reference Projection	1) <b>Yes; Obs. ID 9502</b> 2) Yes; Exposure Weighted Average 3) No; Obs. ID 9502
Source Search (§§3.3 & 4.1)	Search Method; Threshold	1) <b>wavdetect; <math>10^{-6}</math></b> 2) <b>wvdecomp; <math>4.5\sigma</math></b> 3) <b>wvdecomp; <math>4.0\sigma</math></b> 4) <b>R09; <math>4.0\sigma</math></b>
Aperture Photometry (§§3.4, 4.2 & 4.3)	Aperture Size; Background Region	1) <b>Fixed <math>2''</math> radius; the Rest of HRES</b> 2) 95% PSF at 1.5 keV; an Annulus around Each Source
Instrumental Background Model (§§3.5 & 4.4)	Data Set for Modeling	1) <b>Stowed data (Period E)</b> , exposure: 367 ks 2) Stowed data (Period D+E), exposure: 235+367 ks

\*Standard CXC Level 2 event file

source search, and aperture photometry. Calculation of the total resolved X-ray flux requires modeling of the instrumental background in the analysis region. We have created a new analysis pipeline based on a custom analysis pipeline developed over the years for the *Chandra* Multi-wavelength Plane (ChaMPlane) survey (Grindlay et al. 2005)<sup>2</sup>. The latter is described in detail in Hong et al. (2005, H09b). The new analysis pipeline is built on version 4.3 CIAO analysis tools, and has many improvements over the previous pipeline. In particular, we have implemented various analysis approaches with multiple parameter choices including the one similar to what was employed by R09 for comparison. Table 2 summarizes key parameters of analysis approaches used in this paper.

### 3.1 Event Process

The standard CXC<sup>3</sup> pipeline provides Level 1 and 2 event files of each observation. Over the years, there are many subtle or significant improvements proposed and implemented for event processing. In order to identify the effects of these new implementations, we reprocessed the Level 1 event files with a few different options. Two main options considered for reprocessing are pixel repositioning and VF mode cleaning. The pixel repositioning is introduced to reduce pixellation-induced artifacts. For instance, the Energy-Dependent Subpixel Event Repositioning (EDSER) routine is shown to noticeably improve the Point Spread Function (PSF) (Li et al. 2004). The VF mode cleaning reduces instrumental background events by utilizing the  $5 \times 5$  pixel readout of the VF mode (Vikhlinin 2002), but it may also remove some valid events. The Level 2 event files from the standard CXC procedure are generated with the random pixel repositioning under no VF mode cleaning, which is equivalent to the F mode data. We have implemented four approaches as shown in Table 2. Our default choice uses the EDSER routine and the VF mode cleaning for the 2008 observations.

Another minor, but noticeable improvement from the

earlier analysis (Table 1 in H12) is in the Good Time Interval (GTI) selection shown in Table 1. The GTIs are calculated to screen out events acquired during background flares. We consider an interval good if the background rate of the interval is  $< 3\sigma$  from the mean rate. In this analysis, the background rates were calculated from events in the 2.5–7 keV band in 1 ks bins, which is known to be optimal for identifying background flares (Markevitch et al. 2003)<sup>4</sup>. In addition, they were generated after the point source contribution was removed, based on a preliminary source detection by the *wavdetect* algorithm (Freeman et al. 2002). The point source removal keeps the GTI selection algorithm from misrecognizing bright flares of discrete sources as instrumental background flares. For instance, we recovered an erroneously removed 20 min GTIs in Obs. ID 9502 (Hong et al. 2012b). Finally, we also manually verified all the GTIs for any anomaly. As a result, we have removed the full portion ( $\sim 10$  ks) of a background flare in Obs. ID 5934 from the GTIs, only a part of which was identified by the automatic procedure.

### 3.2 Event Merge

We merge the selected events of multiple observations for the full benefit of the ultra-deep exposure. We mainly consider two options in merging: boresight offset correction and the choice of reprojection tangential point. Since the aspect and pointing errors of the *Chandra* observations can be as large as  $0.6''$  (90% confidence)<sup>5</sup>, we use relatively bright X-ray sources detected in each observation for boresight correction (Zhao et al. 2005; Hong et al. 2005). Relative to Obs. ID 5934, the calculated boresight offsets of other observations range from  $0.1''$  to  $0.34''$ . We merged the data with and without the boresight offset correction for comparison.

For the default choice of the common reprojection tangential point, we use the aim point of Obs. ID 9502 with the longest exposure. Since the aim points varied as much

<sup>2</sup> For some of the more recent survey results, see also Servillat et al. (2012); van den Berg et al. (2012a).

<sup>3</sup> <http://cxc.harvard.edu>

<sup>4</sup> Markevitch et al. (2003) recommend using the events of S3 chip in the 2.5–7 keV band for flare identification, but S3 chip was not on for some observations, so we use the events of each CCD in the same energy band.

<sup>5</sup> <http://cxc.cfa.harvard.edu/cal/ASPECT/celmon>



as  $1.3'$  from pointing to pointing (Table 1), we also used the exposure-weighted average aim point of the observations for the reprojection tangential point for comparison.

### 3.3 Source Search

The *wavdetect* routine based on the wavelet algorithm (Freeman et al. 2002) is one of the popular source detection tools in X-ray astronomy. Its performance has been extensively studied and tested (e.g. M03, Kim et al. 2007). We have used the CIAO *wavdetect* routine for source detection for many applications in the past (e.g. Hong et al. 2005, H09b). The *wavdetect* routine delivers a list of sources with detection significance at a somewhat conservative level under the standard parameter setting. Many researchers have developed new techniques or improved the algorithm to catch relatively faint sources missed by the standard *wavdetect* routine, some of which are visually identifiable even in the input images. These include the *wvdecomp* routine by A. Vikhlinin<sup>6</sup>, a multi-statistics based approach by Wang (2004) and an enhanced *wavdetect* algorithm for multiple observations by Kashyap et al. (2011). In particular, the *wvdecomp* algorithm is well suited for detecting faint sources by implementing successive iterations that remove the contribution from bright sources in the image. A typical improvement acquired by these new tools is a  $\sim 10$ – $30\%$  increase in source number under the recommended parameter settings. For instance, M09 found additional  $\sim 26\%$  of sources from the *wvdecomp* routine compared to the sources discovered by the *wavdetect* routine (see §4.1).

Since the final source number counting depends sensitively on some of the input parameters of each detection method, we employ three source detection lists along with the source list from R09 for subsequent aperture photometry. For the *wavdetect* routine, we employ a typical threshold of  $10^{-6}$ , which allows about one false source in each ACIS chip ( $1024 \times 1024$  pixels, see also §4.1.2 & Appendix A). For the *wvdecomp* routine, we have tried two settings of the significance threshold ( $4.5\sigma$  or  $4.0\sigma$ ), which is the main driver of the final source number count. The original prescription of the routine recommends the threshold setting at  $4.5\sigma$ , but R09 lowered it to  $4.0\sigma$  for their analysis under the following two justifications. First, sources only in the high resolution (HRES) region (a central circular region of  $2.56'$  radius) with the highest sensitivity and finest spatial resolution, were considered for analysis. Second, a similar detection run on the instrumental background data produces only 1 or 2 false sources. We will discuss the latter again in §4.1. The number of iterations were fixed at 5 since there is practically no change in source number after the fifth iteration.

### 3.4 Aperture Photometry of Discrete Sources

Aperture photometry can also be applied in many different ways. For the aperture of a given source, we often use a circle around the source position enclosing 95% of PSF for 1.5 keV X-rays, and for the background region, an annulus with the inner and outer radii of  $2\times$  and  $5\times$ PSF respectively. The background annulus region excludes the source

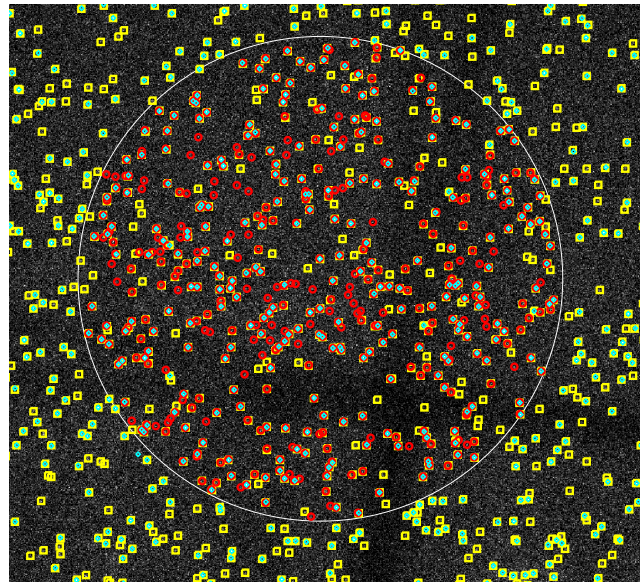


**Figure 1.** The image of the HRES region of the LW marked with sources. The (cyan) diamonds are from the *wavdetect* routine, the (yellow) squares from the *wvdecomp* ( $4.0\sigma$ ), and the (red) circles from R09. See Table 3.

regions of neighbors. This aperture choice allows aperture photometry over the entire field, even outside HRES. R09 used a fixed  $2''$  radius circle around each source for the source aperture and the rest of the HRES region (excluding all the source regions) for the background region. The large, fixed background region provides higher statistics for background counts, but it may not properly reflect a local variation of the background around each source. We employ both approaches for comparison (Table 2).

For background subtraction, we need to know the aperture ratio of the source to background regions. There are a few ways to calculate this ratio; one is a simple geometric ratio of the regions, which is more appropriate for dealing with internal instrumental background, and another is an exposure-map (effective area) corrected geometric ratio of the regions, which is more appropriate for diffuse sky X-ray background. Since both ratios are consistent within less than a percent of each other, here we use the ratio of the exposure-map corrected areas, where the exposure map was generated for 1.5 keV X-rays. Note although the effective area depends sensitively on energies, the ratio of the source to background regions for aperture photometry hardly does. We will discuss the ratio in more detail in §4.4 & Appendix B1.

The frequency of overlapping aperture regions increases, as the source number count increases. In order to avoid double counting of events due to the overlap we uniquely assign each event in the overlapping regions to a source, whose position is closest to the event.<sup>7</sup> The aperture ratio of the source to background regions is adjusted accordingly.

<sup>7</sup> This approach of handling the overlap is different from the equivalent procedure in H05. The latter tries to collect relatively *pure* events, free of contamination from neighbors, but in the process, it drops valid source events if it is highly ambiguous which source they belong to. The new, simple approach counts in all the events in the source regions, which is more appropriate for

<sup>6</sup> <http://hea-www.harvard.edu/RD/zhtools>

**Table 3.** Source Number Counting in the HRES region (2.56' radius) of the LW

(1)	(2)	(3)	(4)	(5)	(6)	(7)	(8)	(9)	(10)
Search	Source	Sources with	Comparison: Sources not found in					Source Number	
Routine	Number	false det. prob.	<i>wvdecomp</i>	<i>wvdecomp</i>	<i>wvdecomp</i>	Ref Coord.		Stowed E	
	0.5–7 keV	<1%	<0.005%	$\geq 4.5\sigma$	$\geq 4.0\sigma$	$\geq 4.0\sigma$ (R09)	Change	9–12 keV	0.5–7 keV
<i>wavdetect</i>	274	274	266	2 (1%)	0 (0%)	5 (2%)	13 (5%)	0	0
<i>wvdecomp</i>									
$\geq 4.5\sigma$	356	355	316	–	0 (0%)	26 (7%)	29 (8%)	2	3
$\geq 4.0\sigma$	439	429	346	83 (19%)	–	75 (17%)	41 (9%)	24	25
$\geq 4.0\sigma$ (R09)	473	456	337	143 (30%)	109 (23%)	–	N/A	N/A	N/A

Notes. (2) The number of sources detected. (3) The number of sources with false detection probability  $P_r < 1\%$  (or detection confidence  $C > 99\%$ ). (4)  $P_r < 0.005\%$  (or  $C > 99.995\%$ ) (see §4.1.2). (5), (6) & (7) The number of unique sources not found by the other search methods in comparison. (8) The number of unique sources compared to the case where the reprojection tangential point was set at the exposure-averaged aim point of the 13 observations instead of the aim point of Obs. ID 9502. (9) The number of sources detected from the image of the LW in the 9–12 keV band. (10) The number of sources from the image of the reprojected Stowed data set (Period E) in the 0.5–7 keV band.

### 3.5 Instrumental Background

In aperture photometry of discrete sources, background subtraction handles both the instrumental and diffuse X-ray background simultaneously. In order to calculate the total resolved fraction, one also has to know the total incoming X-ray flux in the region, which requires an estimate of the total instrumental background in the region. As of this writing, two stowed data sets (Period D and E) are available for modeling the instrumental background of the *Chandra*/ACIS instruments.<sup>8</sup> Period E is from 2005, Oct, 1 to the end of 2009, and Period D is from 2000, Dec, 1 to 2005, Aug, 31. Therefore, the stowed data in Period E is more appropriate for modeling the instrumental background of the observations of the LW. The instrumental background summed over the entire chip is shown to be consistent over the years (Hicox & Markevitch 2006). However, in HRES, both the count rate and the spectral shape of the instrumental background show a noticeable change between Period D and E, which is significant enough to change the overall resolved fraction greatly (Appendix C1). For instance, if Period D stowed data set is used alone, the total resolved fraction of the iron line flux becomes more than 100%, which is in part due to the low statistics of the stowed data set in HRES. We use the stowed data set of Period E alone and the combined set of Period D and E for analysis.

## 4 RESULTS

Here we summarize the results of our analysis in comparison with R09. As we explore several analysis approaches, the results are somewhat extensive. However, they are more or less consistent with a few noticeable exceptions, so we describe the main results based on the default choice of the analysis parameters and point out any significant variations resulted by other parameter choices. The default choice includes the EDSE procedure, the *VF* mode cleaning for the 2008 observations, and the boresight offset correction as listed in Table 2.

estimating the total resolved fraction later, although photometry results may suffer mild contamination from neighbors.

<sup>8</sup> <http://cxc.cfa.harvard.edu/contrib/maxim/acisbg>

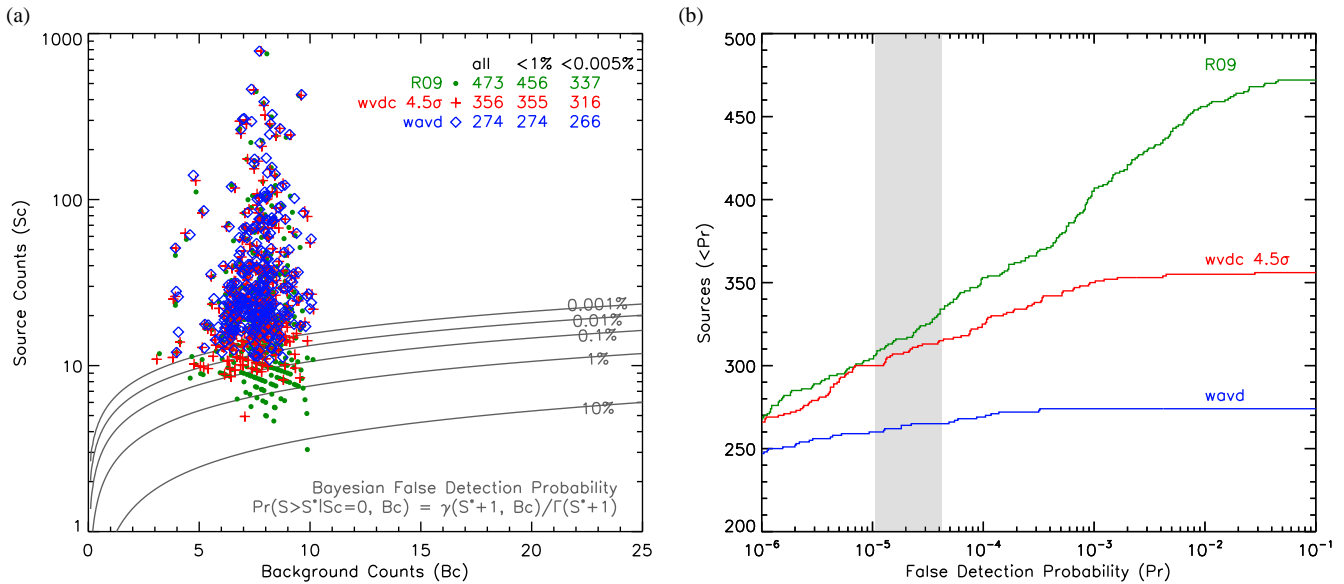
### 4.1 Source Detection

Table 3 summarizes the source search results under the default parameter choice. Two search routines with three parameter choices were applied to the 0.5–7 keV X-ray image of the field (column 2) with the exposure map generated at 1.5 keV. These results are compared with the source number from R09. We detected 251–274 sources from the *wavdetect* routine, depending on how we processed the event files (Table 2). Therefore, R09 detected 70–90% more sources than what the *wavdetect* routine discovered. Compared to our search using the *wvdecomp* routine under the presumably similar parameter settings ( $4.0\sigma$ ) as in R09, R09 still found about 2–6% more sources. Figure 1 shows three of the four search results. In order to evaluate significance of these detections, we take both programmatic and analytic approaches.

#### 4.1.1 Programmatic Approaches

First, we applied the same search routines to the 0.5–7 keV image generated from the stowed data that were reprojected to the sky according to the aspect solution of the observations (column 10). For the analysis with the *VF* mode cleaning, only the events with flag=0 were reprojected in simulating the portion of the 2008 observations. For no *VF* mode cleaning, all the stowed data were reprojected (not shown in Table 3).

The reprojected stowed data can provide a good indicator of false detection rate since they are based on the actual events and the proper dithering motion is included through the reprojection, but there are a few short comings. For instance, the equivalent exposure of the stowed data in Period E is 360 ks, which is a factor of three shorter than the LW data set to reflect the proper Poisson fluctuation for the 1 Ms observation. In addition, events in ACIS-I CCD 1 of the stowed data are artificially generated, based on events in CCD 0. We also note the X-ray flux in the region below  $\sim 5$  keV remained largely unresolved (§4.4, see also R09). Since the image used for source search is generated in the 0.5–7 keV band, the input image for source search routines contains a large diffuse (or unresolved) component besides the instrumental background, which can enhance false detection rate, but the effect of this diffuse sky component cannot be properly accounted for with the stowed data set.



**Figure 2.** (a) Distribution of the source and background counts in detection cells (a  $1''$  radius circle around each source), overplotted with false detection probability ( $P_r$ ) calculated by the Bayesian analysis (Weisskopf et al. 2007; Kashyap et al. 2010). See also Appendix A. (b) Cumulative distributions of the source numbers as a function of  $P_r$ . The shaded region indicates the limit required to ensure 1 or less false source in the source list, assuming that 24k to 96k trials were performed.

Therefore, the source number from the reprojected stowed data set (e.g. 25 in the 439 sources for *wvdecomp* ( $4.0\sigma$ ) in Table 3) represents only a lower limit of the false detections.

The legitimacy of the 473 sources in R09 is in part based on their claim that the same search routine found only 1 or 2 (false) sources on the stowed data set. The stowed data set they used is likely an earlier version of the ones we use and each reprojection generates a different data set in the sky, so there can be some fluctuations from run to run. However according to our analysis, 1 or 2 false detections in the 473 sources of R09 appear to be a severe underestimate.

Second, we applied the search routines to the 9–12 keV image of the LW data (column 9), where no discrete sources are expected to be discovered due to the diminishing effective area ( $\lesssim 10 \text{ cm}^2$ ) and the large PSF. This provides another estimate of the false detections (e.g. 24 in the 439 sources for *wvdecomp* ( $4.0\sigma$ ) in Table 3), but they are still lower limits since the 9–12 keV image also have the similar shortcomings as the stowed data set (e.g. the total number of events in the 9–12 keV band is much smaller than that in the 0.5–7 keV band).

Therefore, we took one more approach to address the false detection rate. We compared the four source lists to find out the objects that are not common to the lists as shown in Table 3 (Columns 5–8).<sup>9</sup> Detection of faint sources near the detection limit is expectedly sensitive to small changes in the

image. For instance, simply changing the image pixellation offset (e.g. 2901.5:5416.5:#2515 vs. 2901.0:5416.0:#2515) or the reprojection tangential point (Column 8) produces a different set of sources under the otherwise identical procedures (i.e. 42 different sources for *wvdecomp* with  $4.0\sigma$  from the tangential point change). Obviously one cannot rule out all of these list-unique sources as invalid, but it is clear that they are prone to small statistical fluctuations of the image and less reliable than the sources consistently detected through these variations. While our source number count (439) did not reach that by R09 (473) under a similar *wvdecomp* run, the comparison of our source list with the list by R09 indicates that about 80–140 sources are in fact unique to each list.

We find a large number of the sources that are not common in our search and R09 in Table 3 puzzling. Are all of these sources, which now add up to  $\sim 550$  objects, valid? To address this, we turn to analytic approaches.

#### 4.1.2 Analytic Approaches

In order to estimate detection significance ( $C$ ) or false detection probability ( $P_r = 1 - C$ ) independent of the source search routines, we employ a Bayesian approach by Weisskopf et al. (2007); Kashyap et al. (2010), which provide a more rigorous treatment of discrete Poisson distributions than simple minded approaches using signal-to-noise ratio (SNR). In Appendix A, we describe a simplified version of the Bayesian approach used for calculating the detection significance and compare it with the SNR based analysis.

Columns 3 and 4 in Table 3 show the number of sources with  $P_r < 1\%$  and  $< 0.005\%$  respectively. The results in Column 3 give a false impression that the majority of these sources are significant. When dealing with a single source or a known source in a new observation, finding the source with

<sup>9</sup> For source match, we employed the prescription by Brandt et al. (2001); M09 with a bit looser requirement by allowing a  $0.5''$  additional offset to compensate for a possible binning effect in the image and source search; i.e. in HRES, when the source separation is more than  $1.1''$ , then they are considered to be different. Therefore, the sources unique to each list Table 3 are usually located in a different section of the HRES region as seen in Figure 1, and they are indeed different sources (not misrecognized as unique to a list because of the pixellation or any other similar effects).



**Table 4.** Aperture Photometry Results of the Resolved Discrete Sources in HRES in the 6.5 – 7.1 and 9 – 12 keV bands

Options / Energy Band	wavd	wvdc (4.5 $\sigma$ )	wvdc (4.0 $\sigma$ )	R09
1) Default	274 sources	356 sources	439 sources	473 sources
Total Events in 6.5–7.1 keV	494 (22)	569 (24)	636 (25)	690 (26)
9.0–12. keV	1642 (41)	2099 (46)	2560 (51)	2818 (53)
Net Photons in 6.5–7.1 keV	295 (22)	316 (24)	328 (26)	355 (27)
9.0–12. keV	23 (41)	32 (47)	34 (53)	55 (55)
2) 1.5 keV 95% PSF with Annulus Bkg.	274 sources	356 sources	439 sources	473 sources
Net Photons in 6.5–7.1 keV	303 (23)	322 (24)	325 (25)	355 (27)
9.0–12. keV	17 (41)	0 (47)	2 (52)	1 (54)
3) <i>F</i> mode	264 sources	354 sources	458 sources	473 sources
Net Photons in 6.5–7.1 keV	308 (25)	322 (27)	349 (30)	366 (30)
9.0–12. keV	–3 (53)	28 (61)	19 (70)	65 (72)
4) No Boresight	267 sources	351 sources	446 sources	473 sources
Net Photons in 6.5–7.1 keV	293 (22)	295 (24)	315 (26)	342 (27)
9.0–12. keV	10 (41)	33 (47)	77 (53)	31 (55)

a confidence level at 99% ( $P_r=1\%$ ) can be considered sufficient to claim a true detection. However, in studying a population of sources newly discovered by a search algorithm, one has to consider the number of search trials explicitly, e.g. 99% confidence means 1 out of 100 *trials* can be false.

The source search routines conduct searches in the entire input images using a small window or detection cell. The cell size is usually smaller than the source aperture region used in aperture photometry for efficient source detection. Following the description of Weisskopf et al. (2007), we assume that a 1'' radius circle is appropriate for the cell size for *Chandra* images especially in the central regions like HRES. The number of independent search trials can be roughly estimated as the ratio of the search region to the cell size. In the HRES region, about 24k independent search trials can be performed. Under 2-Dim Nyquist sampling, these numbers quadruple (96k).

For simplicity we assume each search routine performed 20k trials in HRES,<sup>10</sup> then having a detection with 99% confidence means that there can be as many as 200 false detections arising from random Poisson fluctuations. Note that not all of these 200 sources will be in the source list since each search routine has its own selection criteria to remove false sources. What this means is that sources with 99% confidence have the same significance of other 200 false sources that can be found in the search region. Therefore, in order to make sure the source list contains 1 or less false sources, the required confidence level should be 99.995% or higher (Column 4).

<sup>10</sup> This is a conservative estimate. Our main point, the need for high detection threshold, remains valid as long as the search trials  $\gg 1$ . The precise trial number depends on each algorithm. e.g. *wvdecomp* employs iterations for finding faint sources, so the actual number can be much larger than the ratio of the search region to the cell size. The *wavdetect* routine internally considers each pixel as an independent trial, and the default threshold at  $10^{-6}$  means allowing one false source in 1 Mpixels (1 ACIS CCD). We believe that the detection cell size, which is proportional to the PSF size, should be accounted for in order to get the truly independent trial numbers. However, considering that the two closest sources in the 473 sources by R09 are about a pixel apart, the trial statistics counting scheme in *wavdetect* may be also appropriate for the *wvdecomp* run by R09, in which case there are about 300k trials in HRES.

Figure 2 shows the distribution of source and background counts (see Appendix A) in detection cell (a 1'' radius circle around each source), which is overplotted with various levels of  $P_r$ . The figure also shows the cumulative distributions of the sources as a function of  $P_r$ . The shaded region indicates the limit required to ensure 1 or less false source in the source list, corresponding to 24–96k trials of source search. Figure 2 indicates that  $\lesssim 337$  out of the 473 sources in R09 are detected with sufficiently high significance.

These analytic approaches also often provide only a lower limit of false detection rates due to missing implementation of (usually unknown) subtle features in real data that can give rise to false detections (e.g. source crowding, node boundaries of CCDs or dithering motion induced event scattering). Therefore, we believe the need for detection confidence level more stringent than 99% for source selection remains valid.

In summary, the results in Table 3 indicate that the faintest  $\sim 100$  sources in R09 may not be as significant as R09 claimed. We wonder whether the search parameters in R09 may have been pushed beyond the reasonable limit. On the other hand, our results directly conflict with the aperture photometry results of R09. Figure 3 in R09 indicates a large contribution in the resolved flux in the 6.5–7.1 keV band comes from the faintest sources, which is difficult to imagine if they are mostly false or insignificant detection. We will explore this through aperture photometry in the next section.

## 4.2 Aperture Photometry

Table 4 summarizes the aperture photometry results of the resolved discrete sources in the HRES region. The table shows the summed total events in the source aperture regions and net photon counts after background subtraction in the 6.5–7.1 and 9–12 keV bands for the various analysis options. The default choice uses a fixed 2'' radius aperture around each source for the source region and the rest of the HRES regions (excluding other source apertures) for the background region; the data were prepared and merged with the EDSE procedure, the *VF* mode cleaning and the boresight offset correction. The table compares two aperture photometry methods (Option 1 vs. 2), event selection methods (Option 1 vs. 3), and the effects of the boresight

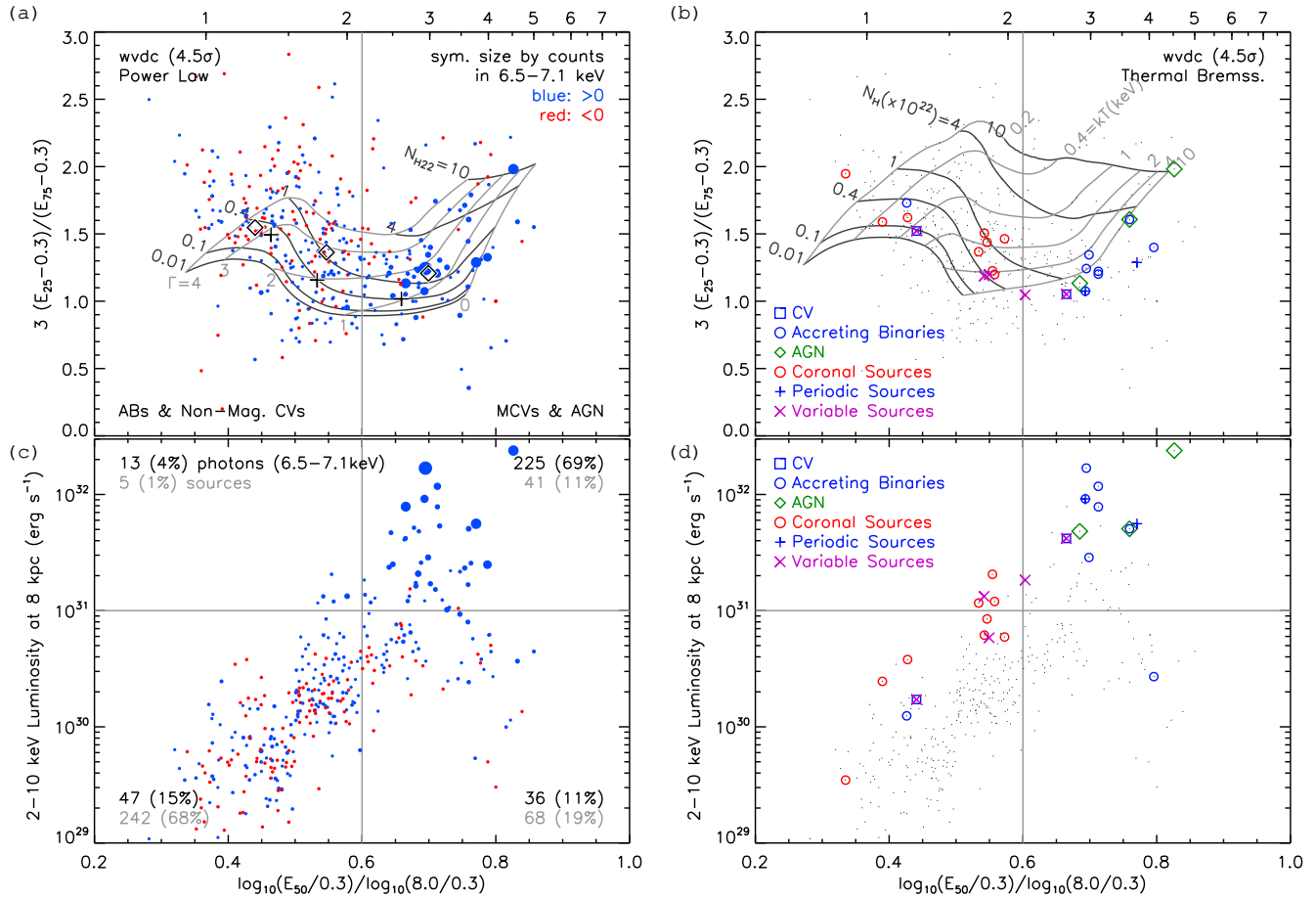


**Figure 3.** X-ray spectral and luminosity distributions of the 356 sources found by the *wvdecomp* (4.5 $\sigma$ ) routine in HRES of the LW. (a) Quantile diagram (Hong et al. 2004, 2009a) overlaid with the power law model grids, and the symbol size is semi-logarithmically proportional to the absolute net counts in the 6.5–7.1 keV band. The blue and red dots represent positive and negative net counts respectively. The diamond and cross symbols represent the combined X-ray spectra of the groups selected by the median values (Q1, Q2 & Q3 in Table 5) and net counts (N1, N2 & N3) respectively. (b) the same as (a) with the thermal Bremsstrahlung model grids, and two dozen sources are marked according to their likely type. (c) & (d) The median energy vs. the 2–10 keV X-ray luminosity at 8 kpc. In (c), the fractional contribution of source number (grey) and the 6.5–7.1 keV net photon counts (black) are noted in each quadrant of the diagram.

**Table 5.** Count to Flux Conversion Factor and X-ray Luminosity by Source Group

(1)	(2)	(3)	(4)	(5)	(6)	(7)	(8)	(9)	(10)	(11)
ID	Selection	QDx	Source Number	Net Photon Counts	Net Photon Counts	$E_{50}$	$N_{H22}$	$\Gamma$	Unabs. Flux	$L_X$ at
	Net			6.5–7.1	0.5–7 keV	(keV)			( $10^{-17}$ )	8 kpc
	Counts									( $10^{29}$ )
Q3	$\leq 300$	$< 0.5$	123	19(10)	4181(89)	1.27(1)	0.31(5)	3.4(2)	0.29	0.22
Q2	$\leq 300$	0.5..0.6	121	37(11)	4098(88)	1.81(2)	1.11(8)	2.8(1)	1.20	0.91
Q1	$\leq 300$	$\geq 0.6$	102	171(16)	5628(94)	2.98(4)	1.5(1)	1.6(1)	2.87	2.19
B	$> 300$		10	95(10)	4364(68)	2.65(4)	0.24(7)	0.86(6)	2.59	1.97
N1	$> 100$		35	203(15)	8583(98)	2.61(3)	0.40(5)	1.04(6)	2.50	1.91
N2	10..100		293	125(19)	9529(137)	1.73(1)	0.37(6)	1.94(8)	1.23	0.94
N3	5..10		19	0(5)	142(26)	1.4(1)	0.3(7)	3(2)	0.49	0.37

Notes. Based on the 356 sources detected by *wvdecomp* (4.5 $\sigma$ ). (1) Group IDs. (3) QDx =  $\log(E_{50}/0.3)/\log(8.0/0.3)$ . It is a normalized logarithmic value of the median energies, x-axis values of the quantile diagram (Hong et al. 2009a). (5) & (6) Summed net photon counts of the sources in the group. (7) The median energy of the combined X-ray spectrum of the group. (8) & (9) Interstellar absorption and power law index of the combined X-ray spectrum of the group under a simple power law model. (10) The unabsorbed 2–10 keV flux in  $10^{-17} \text{ erg s}^{-1} \text{ cm}^{-2}$  for sources with 1 net photon in the 0.5–7 keV band or Conversion factor from the 0.5–7 keV counts to the 2–10 keV unabsorbed X-ray flux in  $10^{-17} \text{ erg s}^{-1} \text{ cm}^{-2} \text{ ph}^{-1}$ . (11) The 2–10 keV luminosity at a distance of 8 kpc in  $10^{29} \text{ erg s}^{-1}$  for sources with 1 net photon in the 0.5–7 keV band.



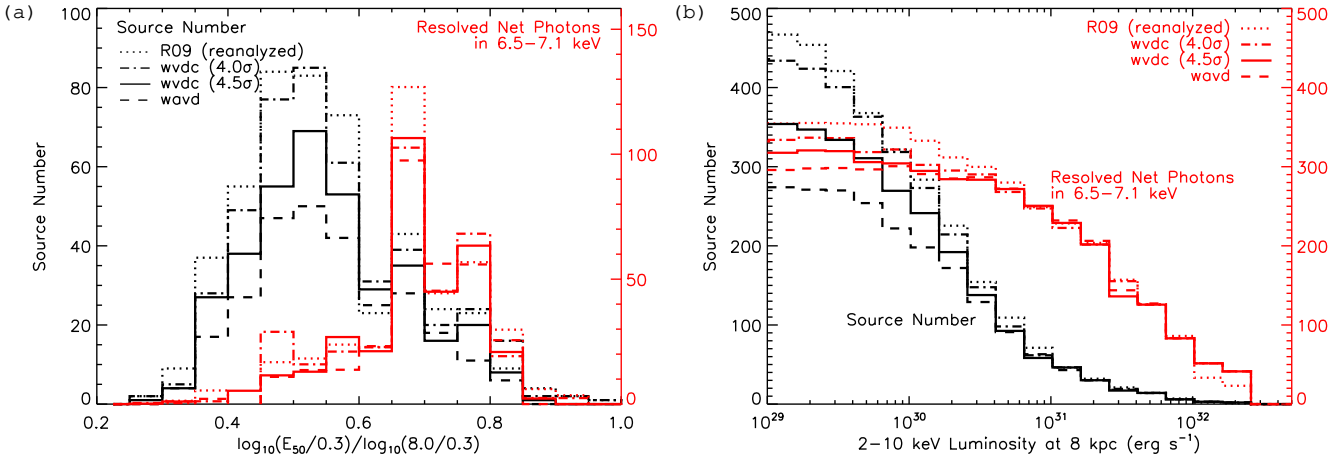


**Figure 4.** X-ray spectral and luminosity histograms of the resolved sources in HRES. (a) Comparison of the source number (black) and 6.5–7.1 keV net count (red) distributions as a function of median energies ( $E_{50}$ ). (b) same as (a), but the cumulative distributions as a function of the 2–10 keV X-ray luminosity at 8 kpc. The results of three different source searches are shown: the 274 sources by *wavdetect* (dashed), the 356 sources by *wvdecomp* ( $4.5\sigma$ , solid), and the 473 sources by R09 (dotted). The majority of the resolved net photons are from the brightest 100–150 sources. Note the faintest ends of the cumulative net count distributions in the 6.5–7.1 keV band alternate positive and negative slopes due to many faint sources with negative net counts in the band.

offset correction (Option 1 vs. 4). For the default choice, we also show the total events in the source region before the background subtraction.

The 6.5–7.1 keV band is chosen to represent the emission lines from highly ionized irons as in R09. The 9–12 keV band results are shown for sanity check: despite the large number of the total events in the source regions in the 9–12 keV band (1642–2818), which are roughly proportional to the number of sources, the summed net photon counts after background subtraction are essentially null, consistent with random Poisson fluctuations as expected.

The four analysis options in Table 4 produce essentially identical results, indicating the outcomes of the aperture photometry are very robust. Only the case with no boresight offset correction (Option 4) produces consistently lower net photon counts for all the four source search routines. While the differences are still within the statistical fluctuations from the other results, the consistent deficit in the net photon counts with no boresight offset correction implies that the boresight offset correction was applied properly in the other options and does improve the aperture photometry.

Unlike the total event counts which are roughly proportional to the number of sources, the total 6.5–7.1 keV net photon counts after background subtraction do not vary significantly among the four source lists. The net photon counts are consistent within  $\sim 3\sigma$ , despite the large differences in the source numbers (e.g. in Option 1,  $295 \pm 22$  photons from the 274 sources by *wavdetect* vs.  $355 \pm 27$  photons from the 473 sources by R09). The source lists by the three *wvdecomp* routines produce the consistent results within  $\sim 2\sigma$ , indicating there is no significant contribution from additional  $\sim 100$  sources found by R09 in comparison to the 356 sources found by the *wvdecomp* algorithm with  $4.5\sigma$ . These aperture photometry results are consistent with the conclusion of the source search results in §4.1: the 50–100 faintest sources in R09 do not contribute significantly in the resolved flux in 6.5–7.1 keV band. This is very different from the conclusion in R09. In order to find the origins of the discrepancy, we ex-

plore the spectral and luminosity properties of these sources in more detail.

### 4.3 Spectral and Luminosity Distribution of the Resolved X-ray Sources

Figure 3 shows the spectral and X-ray luminosity distributions of the 356 sources detected by the *wvdecomp* routine ( $4.5\sigma$ ). These sources are chosen for illustration, and the conclusion remains unchanged for other source search results (see Figure 4). Panels (a) & (b) plot the energy quantiles (Hong et al. 2004, 2009a) of the sources in the same phase space with two spectral model grids (powerlaw and thermal Bremsstrahlung) for comparison. Panels (c) & (d) display the same sources in a phase space of the median energy ( $E_{50}$ , in the 0.3–8 keV band) and the 2–10 keV X-ray luminosity (see below) at a distance of 8 kpc (the Galactic Center). The symbol sizes in (a) & (c) are semi-logarithmically proportional to the absolute counts of net photons in the 6.5–7.1 keV band. The blue and red dots represent positive and negative net counts respectively. Panels (b) & (d) mark a few dozen identified sources or sources with some clue about their nature (V09, H12, Hong et al. 2012b).

#### 4.3.1 Diverse Spectral Types and Flux Calculation

Figure 3 illustrates the diverse spectral types of X-ray sources in the region and the results are very intuitive: the bright, hard X-ray sources mostly contribute the hard X-ray flux. Table 5 also shows the spectral diversity by grouping similar sources. In order to estimate the flux and luminosity of each source in the 2–10 keV band, R09 relies solely on the net counts in the 0.5–7 keV net count rate (see Appendix B3). Both Figure 3 and Table 5 do show a strong correlation between the spectral type and the net counts. However, the spectral diversity present in the same count range of the sources indicates that the count-to-flux conversion factor only based on the counts underestimates the spectral

diversity and misassign the flux values of the sources. Therefore, we group them by the median energy of the sources (only for the sources with less than 300 counts, where the spectral model fit for each source is not reliable). In this way, each group has more or less similar spectral types of sources, and the conversion factor from count rate to flux will reflect their spectral properties. Table 5 shows about a factor of 10 variation in the conversion factor between the softest (Q3) and hardest groups (Q1). It also shows the combined spectrum of the brightest sources (B) is most consistent with the hardest sources (Q1). The 2–10 keV X-ray luminosity at 8 kpc in Figure 3 are calculated using the conversion factors from the net photon counts in the 0.5–7 keV band of three median energies based groups under a simple power law model. For the bright sources with  $\geq 300$  net photons, we use the result of a spectral model fit to each spectrum using a power law model. We have also tried thermal plasma models such as thermal Bremsstrahlung, and for those that produce reasonable fits to the spectra, the X-ray luminosity estimates come out consistent with the one from the power law model.

#### 4.3.2 Sources with Clues

Two best candidate CVs are classified as such based on the blue color,  $H_\alpha$  excess of the optical counterpart, and high  $F_X/F_R$  ratio. Accreting binaries or more marginal candidate CVs are based on the blue color and high  $F_X/F_R$  ratio. Coronal sources are the OGLE-III<sup>11</sup> variables or have bright UCAC2<sup>12</sup> counterparts (see V09 and references therein). Three (candidate) AGN are based on their hard X-ray spectrum and high absorption: one with an extended optical counterpart, another with a very red counterpart and the other with a blue counterpart (i.e. it can also be an accreting binary). These sources are based on the initial 100 ks *Chandra* ACIS-I observations of the LW (V09), and a similar study using the sources from the full 1 Ms exposure is underway (van den Berg et al. 2012b). Two periodic sources found in the region are likely MCVs (H12), one of which is recognized as a candidate accreting binary in (V09). Two of four non-periodic variable sources (flaring or transient) found in the region (Hong et al. 2012b) are also the two best candidate CVs in V09. Periodic or variable X-ray sources are identified from the 1 Ms exposure data.

In the LW outside of the HRES region, a few dozen more sources are either identified or show some clues about their nature (H12, V09). Their distribution shows a similar pattern in the quantile diagram, namely MCVs and AGN are dominantly located at median energy  $E_{50} \gtrsim 2.2$  keV, whereas non-magnetic CVs and coronal sources such as ABs are at  $E_{50} \lesssim 2.2$  keV as illustrated by the vertical gray line in the diagram (see V09, H12). For instance, Figure 9 in H12 shows all 10 MCVs identified in the LW through their periodic X-ray modulation are at  $E_{50} \gtrsim 2.2$  keV. The symbol size and color clearly show the large contribution to the 6.5–7.1 keV flux from the sources located at  $E_{50} \gtrsim 2.2$  keV despite their relative paucity in the diagram (see also Figure 4). In the case of the luminosity distribution, the

**Table 6.** Photon Count in HRES in 3–7, 6.5–7.1 and 9–12 keV

Band Options	Data	Stow E	Stow DE
3–7 keV	All the Events	38412(196)	
VF clean	Reproj. Stowed	10196 (91)	14650 (109)
	Net Photon Counts	11787 (397)	12257 (352)
	*Surface Brightness	492 (17)	514 (15)
6.5–7.1 keV	All the Events	4520(67)	
VF clean	Reproj. Stowed	1531 (35)	2271 (43)
	Net Photon Counts	523 (119)	465 (107)
	*Surface Brightness	77 (18)	68 (16)
9–12 keV	All the Events	34424(186)	
VF clean	Reproj. Stowed	13183 (102)	19282 (123)
	Obs. to Stowed Ratio	2.61 (2)	1.79 (1)
3–7 keV	All the Events	45962(214)	
F mode	Reproj. Stowed	12663 (113)	18206 (135)
	Net Photon Counts	11948 (459)	12169 (406)
	*Surface Brightness	508 (20)	513 (17)
6.5–7.1 keV	All the Events	6698(82)	
F mode	Reproj. Stowed	2254 (47)	3328 (58)
	Net Photon Counts	643 (159)	520 (142)
	*Surface Brightness	95 (23)	77 (21)
9–12 keV	All the Events	58209(241)	
F mode	Reproj. Stowed	21670 (147)	31360 (177)
	Obs. to Stowed Ratio	2.69 (2)	1.86 (1)

\*Surface Brightness:  $10^{-13}$  erg s $^{-1}$  cm $^{-2}$  deg $^{-2}$

dominant contribution to the 6.5–7.1 keV flux comes from the relatively bright sources ( $\gtrsim 10^{31}$  erg s $^{-1}$ ). Panel (c) in figure 3 shows the source fraction and the 6.5–7.1 keV net count contribution of each quadrant in the diagram. The bright, hard sources contribute about 70% of the 6.5–7.1 keV net counts, although they are only about 10% of the total source number.

#### 4.3.3 Sources Resolving Iron Line Flux

Figure 4 shows the spectral and luminosity distributions of the sources found in HRES. Panel (a) contrasts the source number distribution (black lines), which is dominated by the soft sources, with the resolved 6.5–7.1 keV net counts (red lines), which are dominated by the hard sources. The same trends are visible in different source lists by *wavdetect* (dashed lines), *wdecomp* (4.5 $\sigma$ , solid) and R09 (dotted). Panel (b) shows the cumulative source number and 6.5–7.1 keV net counts as a function of the 2–10 keV X-ray luminosity for three source lists. The source number distribution (black lines) are again distinct from the resolved 6.5–7.1 keV net count distribution (red lines). Although comprising a relatively small fraction of the total source number, the relatively bright and hard X-ray sources contribute most of the resolved iron line flux. The small increase in the resolved fraction as the source number counts increases from 274 by *wavdetect* to 473 by R09 can be in part due to a small addition of real sources as expected from the lowered detection threshold (false negatives, see Kashyap et al. 2010). We will address the unresolved spectra in the next section (e.g. Figure 6)

<sup>11</sup> <http://ogle.astrouw.edu.pl>

<sup>12</sup> [http://ad.usno.navy.mil/ucac/u2\\_readme.html](http://ad.usno.navy.mil/ucac/u2_readme.html)

**Table 7.** Resolved Fraction in HRES in 6.5 – 7.1 keV

Fix 2'' Radius Aperture	<i>wavdetect</i>	<i>wvdecomp</i> (4.5 $\sigma$ )	<i>wvdecomp</i> (4.0 $\sigma$ )	<i>wvdecomp</i> (R09)
<i>VF</i> mode clean	(274 sources)	(356 sources)	(439 sources)	(473 sources)
Source to Bkgnd Region Ratio	4.9%	6.4%	7.9%	8.7%
Resolved Fraction (Stow E)	61 $\pm$ 16%	65 $\pm$ 17%	68 $\pm$ 18%	73 $\pm$ 19%
(Stow DE)	68 $\pm$ 18%	73 $\pm$ 19%	76 $\pm$ 20%	83 $\pm$ 22%
<i>F</i> mode	(264 sources)	(354 sources)	(458 sources)	(473 sources)
Source to Bkgnd Region Ratio	4.8%	6.4%	8.3%	8.7%
Resolved Fraction (Stow E)	52 $\pm$ 15%	54 $\pm$ 15%	59 $\pm$ 17%	62 $\pm$ 17%
(Stow DE)	64 $\pm$ 20%	67 $\pm$ 21%	73 $\pm$ 22%	76 $\pm$ 23%

Notes. – For the LW data, which were observed in 2005 and 2008, the Period E stowed data set is more appropriate (§3.5). The results using the Period D stowed data are shown just for comparison to illustrate the dominance of the statistical fluctuation of the instrumental background in the uncertainty of the resolved fraction. See Appendix C1.

#### 4.4 Resolved Fraction of the Iron Emission Lines

Table 6 summarizes the total events and net photon counts in the HRES region in the 3–7, 6.5–7.1 and 9–12 keV bands. The total net photons in the HRES region are calculated by subtracting the instrumental background from the total event counts in the region. The instrumental background counts are acquired from the reprojected stowed events in the same region. For subtraction, we matched counts in the 9–12 keV band.<sup>13</sup> The total measured X-ray surface brightness in HRES is  $I_{3-7 \text{ keV}} = (4.9 \pm 0.2) \times 10^{-11} \text{ erg s}^{-1} \text{ cm}^{-2} \text{ deg}^{-2}$ , which is consistent with the result in R09 ( $(4.6 \pm 0.4) \times 10^{-11} \text{ erg s}^{-1} \text{ cm}^{-2} \text{ deg}^{-2}$ ).

Table 7 shows the total resolved fraction based on Tables 4 & 6. For instance, with the *VF* mode cleaning using the stowed data of Period E, the total net photons ( $N_T$ ) in the 6.5–7.1 keV band in the HRES region are estimated to be  $523 \pm 119$  (Table 6). The resolved 356 sources by *wvdecomp* (4.5 $\sigma$ ) contain  $316 \pm 24$  net photons ( $N_N$ ) (Table 4). This would mean the total resolved fraction of  $61 \pm 15\%$  (vs.  $65 \pm 17\%$  in Table 7), but aperture correction for missing photon counts (loss fraction  $X$ ) due to the finite aperture size needs to be taken into account.

For the fixed 2'' radius PSF, R09 assumed  $X$  to be 10%. However, there are caveats in this assumption when calculating the total resolved fraction and our simulation shows the proper value is about 7% (Appendix B2). After the aperture correction, we get the total resolved fraction of  $65 \pm 17\%$  from the 356 sources by *wvdecomp* (4.5 $\sigma$ ) under the *VF* mode cleaning, using the stowed data of Period E (Table 7). For the 473 sources by R09, we get  $73 \pm 19\%$ . With the combined stowed data set of Period D and E (see Appendix C1, we get  $83 \pm 22\%$ , which is essentially identical to  $84 \pm 12\%$  reported by R09 (before accounting for the unresolved CXB, which is about 4% according to R09, see §5). However, there is a, perhaps critical, difference in the procedure, which is the estimation of ratio of source to background aperture regions ( $r$ ). Table 7 lists  $r$  for each case (8.7% vs. 2% in R09). We will address this issue in Appendix B1 and here we review the results in Table 7.

Various event repositioning methods or aperture choices made little differences. The only major difference comes from the *VF* mode cleaning, which increases the resolved fraction

by about 10–12%. The increase mainly comes from the significant reduction in the total net photons of HRES. For the 473 sources by R09, the *VF* mode cleaning results in 355 net photons in the source regions, which is similar to 366 net photons by the *F* mode (Table 4). On the other hand, in the HRES region as a whole, the *VF* mode cleaning produces 523 net photons as opposed to 643 photons by the *F* mode. The two results are consistent within  $1\sigma$  due to the large errors, and these large statistical errors dominate the uncertainty of the total resolved fraction. Projecting from the count decrease by 11 in the source region by the *VF* mode cleaning<sup>14</sup>, we estimate that the total real photons removed by the cleaning in HRES is about 19.<sup>15</sup> In other words, at least about 80% of 100 events removed by the *VF* mode cleaning are indeed background events.

Note the total resolved fraction has a relatively larger error compared to net photon counts in the source regions due to the additional uncertainty of the instrumental background subtraction. The uncertainty of the instrumental background is dominated by the relatively poor statistics of the stowed data in comparison to the 1 Ms observation (the count ratio in the 9–12 keV band between the two is 2.6, as shown in Table 6). The dominance of the stowed data in the error budget becomes clear when the Period D data set is used; more than 100% is resolved (not shown), which is improbable (see Figure 8 and Appendix C1 for more about large variations between the two stowed data sets).

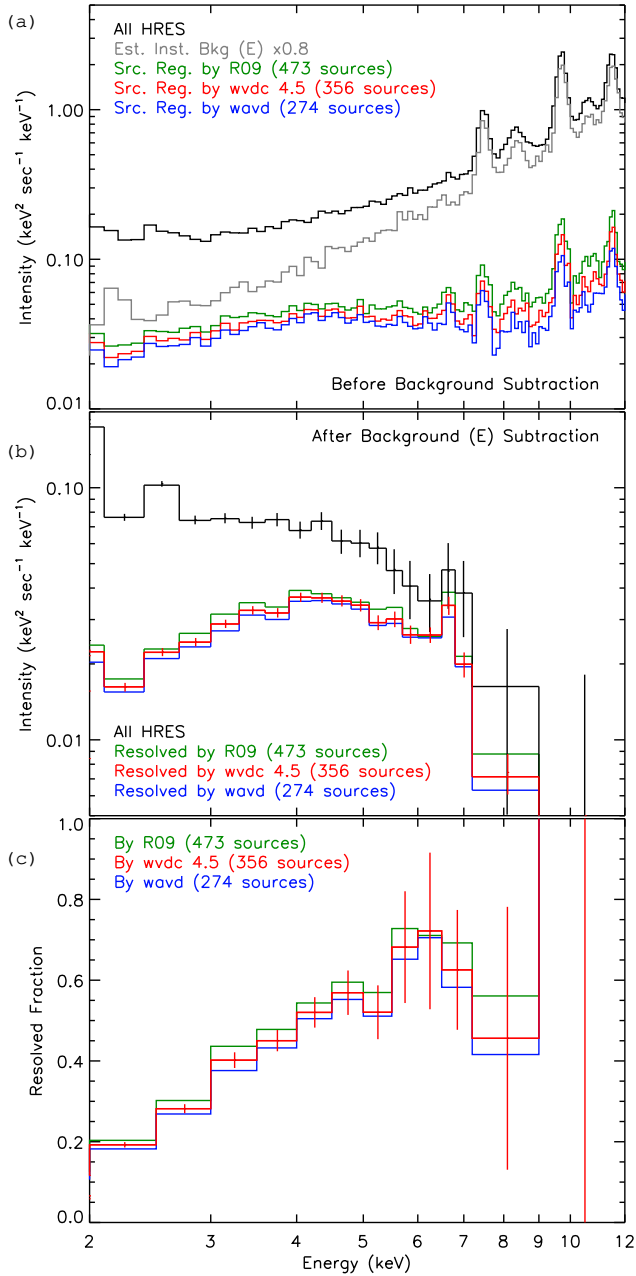
Figure 5 shows the total net spectrum of HRES, the resolved spectrum, and the resolved fraction as a function of energy and compare their results with three source search routines. Both Table 7 and Figure 5 show that the additional  $\sim 100$  sources added by R09 (or by the *wvdecomp* routine at 4.0 $\sigma$ ) relative to the 356 sources from the *wvdecomp* routine at 4.5 $\sigma$  do not contribute significantly to the resolved X-ray flux in the iron emission lines and the 2–9 keV band in general.

Figure 6 shows the resolved spectrum and fraction for soft ( $E_{50} < 2.2 \text{ keV}$ ) and hard ( $> 2.2 \text{ keV}$ ) sources. There is a clear disparity in the combined spectrum between the hard (blue) and soft (red) sources, which is consistent with the large variations in count-to-flux ratio conversion factors between the different spectral groups in Table 5. The large

<sup>13</sup> This is identical to the procedure in R09, although in R09 the count rate in the 9–12 keV band is matched instead of the counts. It is because their subtraction is done in count rate space and ours in count.

<sup>14</sup> Compare the net photons (355 vs. 366) in 6.5–7.1 keV between 1) and 3) of the R09 column in Table 4

<sup>15</sup> Using the ratio of the total net photons in HRES (*F* mode in Table 6) to the net photons in the source region for 3) of R09 in Table 4:  $11 \times 643/366$ .



**Figure 5.** GRXE spectrum and resolved fraction. (a) The X-ray spectrum before background subtraction, (b) the X-ray spectrum after background subtraction, and (c) the resolved fraction as a function of energies. The total spectrum in HRES and the results for three source lists are shown. In (a), the estimated instrumental background is shown in grey (scaled by 0.8 for clarity) and the spectra for the source regions are not corrected for event loss due to the finite PSF size. In (b) & (c), the event loss is corrected (see the text). The results are based on the default parameter choice (the EDSE routine, the *VF* mode cleaning, the Period E stowed data set, and fixed  $2''$  radius source apertures).

majority of the resolved fraction above 3 keV comes from the hard sources, which are likely MCVs and AGN, whereas the soft sources such as ABs and non-magnetic CVs contribute about 15% or less. See also Appendix C2. Among the additional 117 sources in R09 relative to the 356 sources from

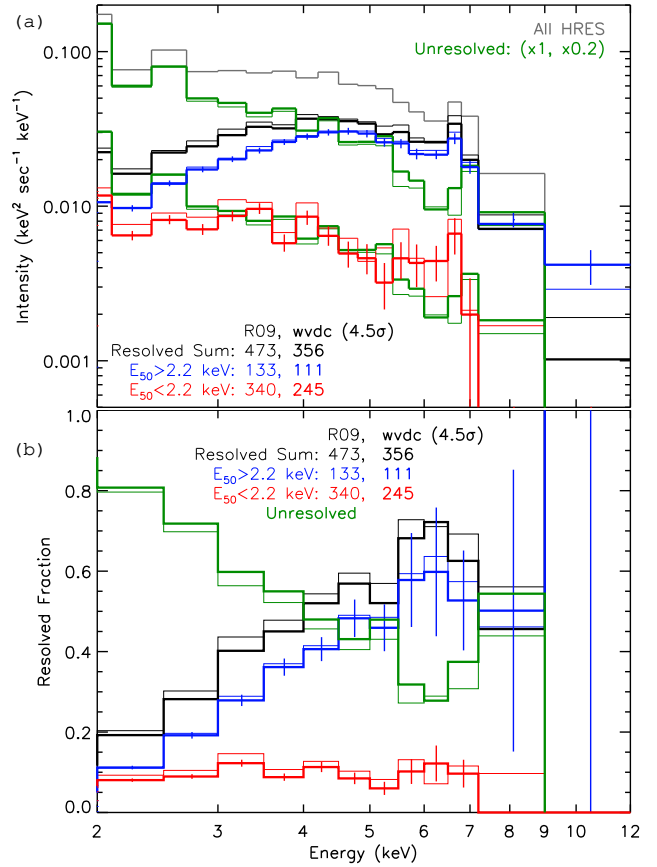


**Figure 6.** The same as Figure 5 for two source lists by *wvdecomp* ( $4.5\sigma$ , thick lines) and R09 (thin lines). The contribution from the resolved discrete sources are broken up by the soft (red,  $E_{50} < 2.2$  keV) and hard (blue,  $E_{50} > 2.2$  keV) sources. The residual unresolved X-ray spectrum and its twin scaled by 0.2 are shown in green for comparison with the X-ray spectra from the hard and soft sources. Among the additional 117 sources in R09 relative to the 356 sources from *wvdecomp* ( $4.5\sigma$ ), the increase in the resolved fraction above 5 keV is mainly from the 22 hard sources rather than the 95 soft sources.

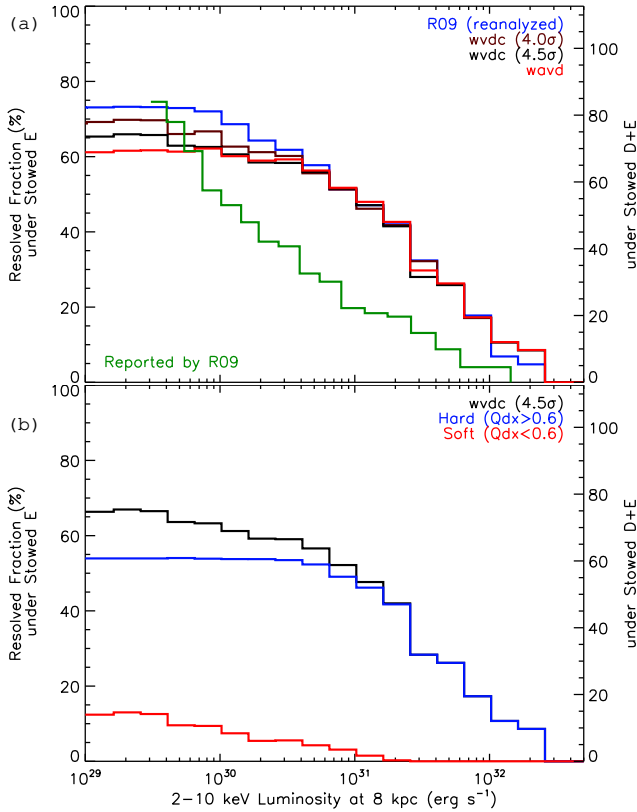
*wvdecomp* ( $4.5\sigma$ ), the increase in the resolved fraction above 5 keV is mainly from the 22 hard sources rather than the 95 soft sources, although the increase is within the statistical uncertainty. This implies that if indeed some real sources are added by lowering the detection threshold between these two source lists, they are mainly in the hard X-ray sources, and the trend of the dominance of the hard X-ray sources in the 6.5–7.1 keV band continues at low fluxes.

Figure 7 shows the X-ray luminosity distribution of the resolved fraction in comparison with the results of R09. Our analysis shows the faint sources do not contribute significantly to the resolved fraction (See also Appendix C3).

## 5 DISCUSSION

Our estimate of the total resolved fraction ( $73 \pm 19\%$  under Period E or  $83 \pm 19\%$  under Period D+E) in the 6.5–7.1 keV band in HRES from the 473 sources found by R09 is consistent with the estimate by R09 ( $84 \pm 12\%$  under Period D+E) within the large uncertainties. However, our results





**Figure 7.** The resolved 6.5–7.1 keV flux as a function of the 2–10 keV luminosity at 8 kpc. (a) The total resolved fractions by three source lists are compared with the result by R09. (b) The contribution from the hard and soft sources are separated out for the 356 sources by *wvdecomp* ( $4.5\sigma$ ). Note the hard sources reaching the plateau at higher luminosity is due to the higher sensitivity limit for the hard X-ray sources (see Figure 3).

regarding source search, aperture photometry, and the resolved fraction, all consistently indicate that the relatively bright, hard X-ray sources such as MCVs and AGN contribute  $\sim 80\%$  of the resolved flux, more dominantly than the faint, soft X-ray sources such as ABs and non-magnetic CVs, which contribute  $\lesssim 20\%$ . Subsequently our results indicate the faintest  $\sim 100$  sources found by R09 are insignificant. Therefore, we consider the results from the 356 sources by *wvdecomp* ( $4.5\sigma$ ) is more reliable, and we can confidently claim that the resolved fraction in HRES is  $65 \pm 17\%$  (Period E) or  $73 \pm 19\%$  (Period D+E). Assuming the unresolved CXB in the 6.5–7.1 keV flux to be  $2.9 \times 10^{-13} \text{ erg s}^{-1} \text{ cm}^{-2} \text{ deg}^{-2}$  (R09), which is about 3–4 % of the total intensity (Table 6), the total resolved fraction of the 6.5–7.1 keV flux in HRES is  $69 \pm 17\%$  (Period E) or  $77 \pm 19\%$  (Period D+E). This result is also roughly consistent with  $88 \pm 12\%$  by R09, but unlike R09, our finding of the dominance of relatively bright, hard X-ray sources in the resolved fraction draw a drastically different picture in the source composition and strongly motivate the analysis beyond HRES and the LW.

First, our finding is consistent with the previous studies indicating MCVs are likely major candidates for the low luminosity Bulge hard X-ray sources (e.g. M03, M09, H09b). These studies also found a hint of an excess of hard X-ray sources in the central Bulge relative to stellar popu-

lation models. On the other hand, Revnivtsev et al (2006); Revnivtsev & Sazonov (2007); Revnivtsev et al. (2009) argue the similarity of the Galactic distribution of the GRXE and the IR flux, which follows the stellar population. This apparent inconsistency is in part due to the relative shallow survey of the previous studies ( $< 100 \text{ ks}$ ).<sup>16</sup> The excess of the hard X-ray sources is only observed in the very central Bulge within a few arcmin of Sgr A\*, given the shallow exposure of the large survey (e.g. M09, H09b). The overall X-ray flux used to match with the IR flux is still dominated by the soft X-ray contribution, which is largely unresolved and may not trace the hard X-ray sources. Therefore, the hard X-ray emission of the GRXE can be mainly from a relatively small number of hard X-ray sources, and the above apparent inconsistency can be explained by the fact that these previous studies were tracing a different population of X-ray sources.

Second, if indeed relatively bright, hard X-ray sources dominate the iron emission line flux of the GRXE, we should be able to resolve a large fraction of the same emission line in the region beyond HRES despite some sensitivity loss due to the large offset. This argument also applies to the Galactic plane fields with relatively high extinction if a similarly ultra-deep exposure is available. Then with the majority of the hard X-ray emission in the GRXE being resolved, we are positioned to investigate the possible variation of X-ray source composition between the fields and Bulge, which can provide a hint in the unique formation and evolutionary history of the Bulge. Extending the analysis beyond HRES also allows a significant reduction of the uncertainty in the resolved fraction by improving the instrumental background statistics of the stowed data set, which is the dominant source of the uncertainties (Appendix C1).

In the following, we extend our analysis beyond HRES in light of our new results and discuss future observations and analysis plan to improve our understanding of the spatial variance of the source composition and the GRXE (see also Morihana et al. 2012). Finally, we summarize our thoughts on the origin of the discrepancy between our results and R09 and some of the analysis caveats in the Appendix (B & C).

## 5.1 Beyond HRES

Figure 8 shows the source number density, net photon counts, and the resolved fraction of the 6.5–7.1 keV flux as a function of the radius from the center of HRES using the resolved sources from the *wvdecomp* routine ( $4.5\sigma$ ). The figure also shows the hard (blue) and soft (red) sources separately, and the results with (solid) and without (dotted) the *VF* mode cleaning. For a given source, we use the 1.5 keV 95% PSF for the source region and the surrounding annulus for the background region for aperture photometry since the fixed  $2''$  radius aperture is no longer applicable at large offset angles and using the rest of HRES (excluding the source regions) for the background region does not reflect the local variation of background. The use of variable

<sup>16</sup> We do not consider the possibility of inaccurate modeling of stellar population or the disparity between the stellar population and the IR flux, both of which are outside of this analysis.

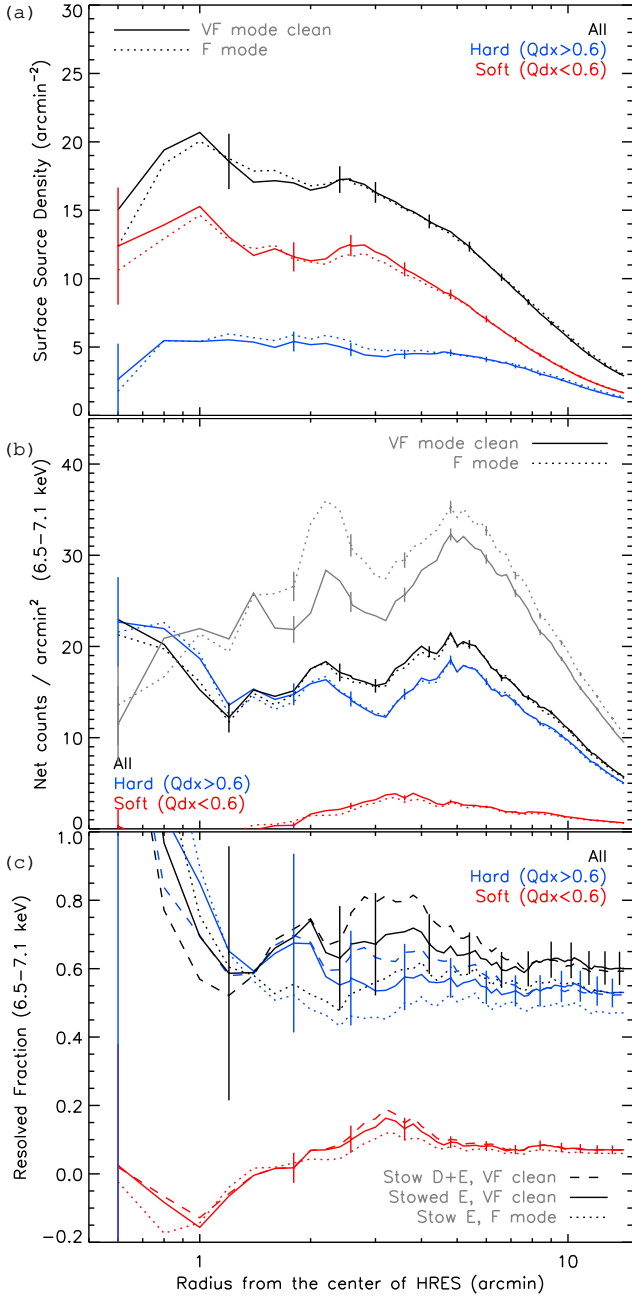


**Figure 8.** Radial distribution of (a) the source surface density, (b) the net photons in the 6.5–7.1 keV band within the given radius, and (c) the resolved fraction using the sources detected by *wvdecomp* ( $4.5\sigma$ ). Source apertures are 1.5 keV 95% PSF and the background apertures are the surrounding annulus ( $2\times$  and  $5\times$  of the PSF radius for inner and outer radii respectively). The solid lines are for VF mode cleaning and the dotted lines for F mode. The soft (red) and hard (blue) sources are separated based on the median energies.

apertures is justified since in HRES both cases of the aperture choices (variable and fixed sizes) produce the consistent results (Table 4 Options 1 vs. 2).

As expected, the surface density of the soft sources (red in Figure 8a) show a more significant change with the radius of the analysis region than that of the hard sources (blue in Figure 8a). The former drops noticeably beyond  $2.5'$  from

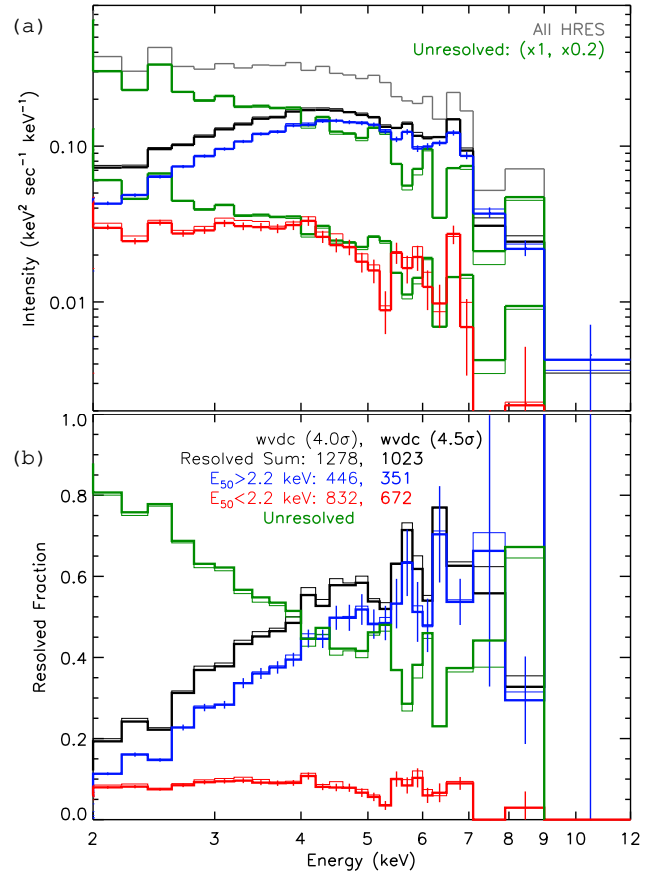


**Figure 9.** The GRXE and resolved spectra (a), and the resolved fraction (b) in the central region within the  $5'$  radius (using the Period D+E stowed data set). The results are shown for two source lists by *wvdecomp* ( $4.0\sigma$  for thick lines and  $4.5\sigma$  for thin lines). The grey line is for the GRXE spectrum, and the black lines are the resolved X-ray spectrum. The blue and red lines are the resolved spectra from the hard and soft sources respectively. The green lines show the unresolved spectra and their scaled twins ( $\times 0.2$ ) for comparison with the combined spectra of the soft X-ray sources. Compare this with Figure 6.

the center, whereas the latter are more or less uniform out to  $5'$ . The similar trend can be seen in the total net photons in the 6.5–7.1 keV band from the hard X-ray sources (blue in Figure 8b) and the analysis region altogether (grey in Figure 8b), which peaks at around  $5'$ . On the other hand, the 6.5–7.1 keV photons from the soft X-ray sources (red in Figure 8b) rises up and peaks at  $3.5'$  and drops afterwards, which can be partially explained by a patch of seemingly diffuse soft emission region at around  $3-4'$ .

The contribution to the resolved fraction from the soft sources are insignificant throughout the field. In fact their contribution in the very central region is non-existent despite the relatively large number of sources found in the region. This again supports our finding of the dominance of the relatively bright, hard X-ray sources in the resolved GRXE. It is also consistent with a recent independent analysis of the region by Morihana et al. (2012). In the case of the resolved fraction, the radial variation is not significant, but its uncertainty drops noticeably as extending to the larger region. If we limit our analysis to  $5'$  where the total net

photon density in the 6.5–7.1 keV band of the analysis region is highest, the resolved fraction is  $64 \pm 6\%$  (Period E) or  $69 \pm 7\%$  (Period D+E) for *wdecomp* ( $4.5\sigma$ ); after including the 3.7% CXB contribution, the total resolved fraction is  $68 \pm 6\%$  (Period E) or  $73 \pm 7\%$  (Period D+E).<sup>17</sup>

## 5.2 Unresolved GRXE

Figure 9 shows the GRXE and its resolved spectra in the  $5'$  radius region. The result is consistent with that in HRES (Figure 6). Now with higher statistics, one can see a few more features in the spectra. First, there appears to be a lack of the 6.4 keV emission line in the region (e.g. see the black lines in the 6–6.5 keV band in Figure 9a). Although the ACIS CCD spectral resolution in HRES may not be suitable for clear separation of the 6.4 and 6.7 keV lines under the given relatively poor statistics (cf. Ebisawa et al. 2008), other Bulge fields such as the Galactic center strip surveyed by Wang, Gotthelf & Lang (2002) show a prominent emission line feature at 6.4 keV, a large fraction of which may be of diffuse origin. Second, the spectra from the resolved sources, in particular, the soft sources, shows an absorption feature in the 5–5.5 keV band. In turn, the unresolved spectrum (green) shows an emission feature in the same energy band.

Given high stellar density in the LW, where often more than a few stars with  $V \lesssim 24$  within the error circle of X-ray positions are observed in the *HST* image (V09), it is still possible that the unresolved 20–30% can be from the X-ray emission of the unresolved discrete sources. The relatively soft X-ray spectrum of the unresolved residual GRXE (green in Figures 6 & 9) suggests a possibility that the unresolved discrete sources are mainly soft coronally active stars such as ABs. In fact, the unresolved spectrum is clearly softer than the combined spectrum of the soft sources, so there may be more contribution from ABs than non-magnetic CVs in the unresolved spectrum, whereas the resolved spectrum of the soft sources may have relatively larger contribution from non-magnetic CVs. This interpretation is consistent with ABs and other coronally active sources being fainter ( $\sim 10^{28-31}$  erg s<sup>-1</sup>) than accreting sources such as non-magnetic CVs ( $\sim 10^{29-32}$  erg s<sup>-1</sup>), but it also implies the contribution from ABs is not resolved at this luminosity limit.

Alternatively it is also possible that the hard X-ray flux ( $> 4$  keV) of the unresolved GRXE is mainly from the faint hard X-ray sources such as MCVs and the soft flux from the coronally active stars like ABs. For instance, the X-ray spectrum of the unresolved CXB ( $\sim 4\%$  of the total flux in the 6.5–7.1 keV band) can be described by a power law spectrum with photon index of 1.4. In other words, the combined unresolved spectrum (green) in Figures 6 & 9 contains a contribution from the sources whose spectra are much harder than the combined unresolved spectrum itself or the combined spectrum of the soft sources. If the 8% increase in

the resolved fraction of the 6.5–7.1 keV band from the 356 sources by *wdecomp* ( $4.5\sigma$ ) to the 473 sources by R09 is credible (thick to thin lines in Figure 6), the latter scenario is supported by the fact that most of the 8% increase is from the faint hard X-ray sources but not from the faint soft X-ray sources. Then the paucity of the hard X-ray sources implies a truly diffuse hard X-ray component may be present in the GRXE.

## 5.3 Future Studies

It is now possible to draw a rather complete picture of the Galactic X-ray source composition and their Galactic distribution, through resolving the majority of the GRXE by ultra-deep *Chandra* exposures. This calls for more observations and analysis of the other fields. The LW field, while perhaps ideal for resolving the GRXE due to the proximity to the GC and the low extinction, may not represent a typical Bulge field in the Galactic Plane. First, the total X-ray spectrum of the LW field lacks the neutral Fe 6.4 keV emission line, which is often outstanding in the Plane fields and suspected to be mainly from the diffuse emission (e.g. Wang, Gotthelf & Lang 2002). Therefore, an ultra-deep exposure of the Plane fields (apart from the Sgr A\* field, which contains many complex diffuse features) is required. Second, unlike the Fe 6.7 keV line, the 2–6 keV medium-hard flux remains largely unresolved. As seen in the previous section, comparison of the unresolved GRXE spectrum with the combined spectra of the soft and hard X-ray sources may indicate spectral transitions from hard MCVs, to soft non-magnetic CVs, and to even softer, unresolved ABs (or diffuse components). Therefore, the medium band GRXE and its spatial variation will allow modeling of the relative composition of the three major source types. For this, another low extinction field such as Baade’s Window (BW) at  $4^\circ$  south of the GC might be ideal. For instance, unlike the LW, in BW the apparent diffuse X-ray emission is remarkably absent. The lower extinction and the lack of the apparent diffuse emission in BW improve a chance of resolving the GRXE in a broader band than in the LW. In addition, unlike the hard X-ray sources whose density falls radially from the GC, there is an excess of the soft X-ray sources in BW relative to the LW at the same 100 ks exposure (H09b), despite the larger offset of BW from the GC ( $4^\circ$  vs.  $1.4^\circ$  for the LW). Therefore, when the spatial variance of the GRXE between BW and the LW is compared to the variance of the hard and soft X-ray source numbers, the unambiguous contribution of each source type to the GRXE can be calculated.

The wide band coverage (5–200 keV) and large effective area ( $\gtrsim 700$  cm<sup>2</sup> at 7–12 keV) of the Nuclear Spectroscopic Telescope Array (NuSTAR) (Harrison et al. 2005) bring a new promise of constraining the GRXE. A mildly deep observation (e.g. 200 ks<sup>18</sup>) of the LW with NuSTAR will enable the absolute intensity measurement of the GRXE in the region above 6 keV. Such a measurement will allow a precise calculation of the resolved fraction of the GRXE by the

<sup>17</sup> The total resolved fraction does not change significantly even out to  $10'$ . This is because the X-ray flux at large off-axis angles does not contribute significantly due to the reduction in the effective area. Subsequently there is no improvement in the uncertainty of the total resolved fraction.

<sup>18</sup> This is actually much deeper in the hard X-ray band ( $> 7$  keV) than the 1 Ms *Chandra* exposure since the effective area of *Chandra* is less than 100 cm<sup>2</sup> above 7 keV.

*Chandra* sources without relying on the somewhat uncertain *Chandra*/ACIS instrumental background.

## 6 SUMMARY

Through an independent analysis of the X-ray sources in the LW, we resolved the iron emission line of the GRXE in the 6.5–7.1 keV band up to  $(69\text{--}77) \pm 19\%$  in the central circular region of 2.56' radius<sup>19</sup> and  $(65\text{--}73) \pm 7\%$  for the 5' radius. The dominating uncertainty is from the instrumental background in both statistical and systematic nature (e.g. *VF* mode cleaning, Period D+E vs. E). We find that the resolved GRXE is dominated by the relatively bright ( $\gtrsim 10^{31}$  erg s<sup>−1</sup>), hard X-ray sources ( $E_{50} \gtrsim 2.2$  keV), which are likely MCVs and AGN. The relatively faint, soft X-ray sources such as ABs and non-magnetic CVs do not contribute more than 20% of the resolved flux. The refined resolved fraction in the 5' radius region leaves room for truly diffuse components in the GRXE, but the undetected large population of the relatively faint ( $\lesssim 10^{31}$  erg s<sup>−1</sup>), hard X-ray sources can make up for the unresolved fraction. We also believe we have identified a few analysis caveats in R09, which led to the disagreement with our results regarding the source composition of the resolved GRXE.

## 7 ACKNOWLEDGEMENT

We thank M. van den Berg and M. Servillat for reading the manuscript and useful comments. We thank V. Kashyap for his help on calculation of detection confidence. We also thank M. Revnivtsev for providing his source list and the extensive discussion on the topic and analysis despite some disagreement in the results. We also thank J. Grindlay for his support and useful suggestions in the analysis.

## APPENDIX A: DETECTION SIGNIFICANCE

Detection significance is often estimated based on signal-to-noise ratio (SNR). If the background count ( $B_C$ ) in the detection cell ( $\Omega_T$ ) is known, the SNR to describe detection significance<sup>20</sup> is given as  $S_C/\sigma_{B_C}$ , where  $S_C$  are the photon counts from the source and  $\sigma_{B_C}$  is the fluctuation of the background counts. For Poisson distribution,  $\sigma_{B_C}$  is simply  $B_C^{0.5}$  or  $1 + (0.75 + B_C)^{0.5}$  at low counts ( $\lesssim 15$ ) (Gehrels 1986). The SNR-based approaches involve a number of approximations: for a given confidence ( $C$ ) or a false detection probability ( $P_r = 1 - C$ ), it is often assumed that the SNR follows a Gaussian distribution. For instance, for >90% confidence ( $P_r < 0.1$ ) with  $B_C = 1$ ,  $S_C > 1.28$  (SNR > 1.28)

<sup>19</sup> This is from *wvdecomp* ( $4.5\sigma$ ) under the *VF* clean mode in Table 7, including  $\sim 4\%$  of the unresolved CXB. For singling out this result, see §5.

<sup>20</sup> Note the difference from the SNR often used to describe the confidence range of the source count, where the noise term includes the error contribution of the source count as well. e.g. when the error of the background count is estimated independently,  $\text{SNR} = S_C/(\sigma_{T_C}^2 + \sigma_{B_C}^2)^{0.5}$  where  $T_C$  is the error of the total counts in the source region.

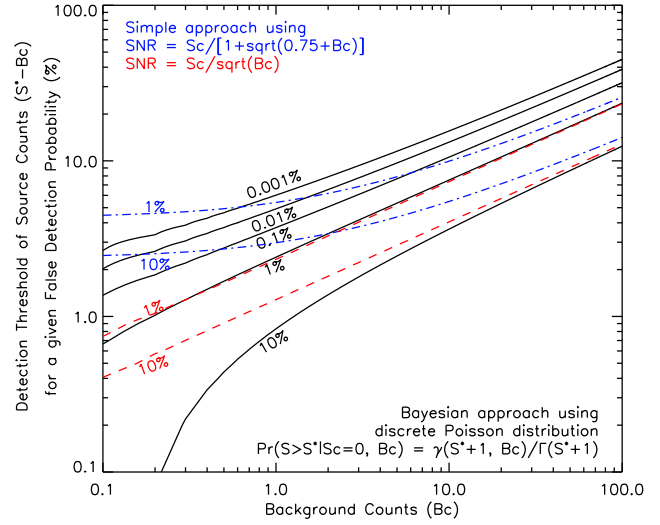


**Figure A1.** Detection threshold ( $S^* - B_C$ ) for source count under a given false detection probability ( $P_r = 1 - C$ , where  $C$  is the detection confidence). The simple minded approaches using signal-to-noise ratios (SNRs) (red dash for Gaussian statistics & blue dotted-dash for Gehrels' approximation for Poisson statistics) is compared with the Bayesian approach (black solid) by Weisskopf et al. (2007); Kashyap et al. (2010). Note  $P_r$  from the Bayesian analysis is defined for the total counts ( $S$ ) in the detection cell (see Figure 2 in Kashyap et al. (2010)), so technically the Bayesian approach does not provide the detection threshold for source counts ( $S_C$ ), but for easy illustration of how bright the source needs to be for detection, the detection threshold is expressed for  $S_C$  under the assumption that  $B_C$  is known (subsequently the plot ignores the discrete nature of the counts as well). Ironically using the SNR based  $P_r$  under Gehrels' approximation without accounting for trial statistics can underestimate the false detection probability for high background cases.

or  $S_C > 2.97$  for Gehrels' approximation, see red and blue lines in Figure A1).

A more rigorous approach based on discrete Poisson distributions and a Bayesian treatment of false detection probability can be found in the literature: Eq. A11 in Weisskopf et al. (2007) (see also Eq. A8) and footnote 13 in Kashyap et al. (2010). Their formulae are identical<sup>21</sup> to each other except for their interest of unmarginalized parameters: the cell size ( $\Omega_T$ ) in the former and the exposure ( $\tau_S$ ) in the latter. If we assume  $B_C$  is measured, the false detection probability is simplified as

$$\begin{aligned} P_r(S > S^* | S_C = 0, B_C) &= 1 - C \\ &= \sum_{m=0}^{S^*} \frac{B_C^m}{m!} e^{-B_C} \\ &= \frac{\gamma(S^* + 1, B_C)}{\Gamma(S^* + 1)}, \end{aligned}$$

where  $\gamma$  and  $\Gamma$  are incomplete and regular gamma functions

<sup>21</sup> Note that there is an error in the formula in footnote 13 of Kashyap et al. (2010):  $\gamma(S^* + 1, \tau_S \lambda_B) = \int_0^{\tau_S \lambda_B} e^{-t} t^{S^*} dt$ .



respectively. Under this approach, for  $> 90\%$  confidence with  $B_C = 1$ ,  $S_C > 0.8^{22}$  (see black lines in Figure A1).

We use a circular region of  $1''$  radius around each source for detection cell, following Weisskopf et al. (2007), and calculate the source counts ( $S_C$ ) by subtracting the background counts ( $B_C$ ) from the total counts ( $S$ ) in the cell. For the background counts ( $B_C$ ), we take the counts in an annulus around the source with  $4''$  and  $10''$  radii (excluding the  $3''$  radius circles of neighboring sources), and scale them by the ratio of the detection cell size to the background region. Here we assume that  $B_C$  represents the true mean value of the background counts in the detection cell for simplicity. The range of  $B_C$  for the sources in HRES is 3.1 to 21. Note the detection cell is chosen to be smaller than the source aperture regions in aperture photometry (§3.4), since the former is designed for efficient source detection and the latter is designed for accurate flux estimation.

Figure A1 compares the two approaches under the assumption that  $B_C$  is known. Gehrels' approximation is often used to account for the asymmetric deviation of Poisson distributions from Gaussian distributions at low counts ( $\lesssim 15$ ). However, Figure A1 shows in fact using simple Gaussian errors is more accurate than using Gehrels' approximation, indicating the latter may result in detection loss of faint sources. On the other hand, the real data can often deviate from a pure Poisson distribution or contain features that are not easy to account for, and thus it is usually a safe approach to have a higher threshold by using Gehrels' approximation.

For detection confidence of a population of sources discovered by a search routine, one has to take into account the number of search trials explicitly. Without accounting for trials statistics, both simple Gaussian errors and Gehrels' approximation of Poisson errors result in a wrong estimate of false detections. Ironically using Gehrels' approximation without accounting for trial statistics may accidentally produce a proper estimate of false detections at low background count cases but it will underestimate false detections at high background count cases. e.g. in Figure A1, the detection threshold for  $P_r=1\%$  using Gehrels' approximation (the blue line) matches the threshold for  $P_r=0.01\%$  from the Bayesian approach (the black line) when  $B_C \sim 1$ , but the threshold for the former is lower than the latter when  $B_C \gtrsim 2$ .

## APPENDIX B: ORIGIN OF DISCREPANCY IN APERTURE PHOTOMETRY

In our opinion inaccurate estimations of the following three quantities in R09 are the major origins of the discrepancy between R09 and ours in the aperture photometry results.

### B1 Source to Background Region Ratio

Table 7 shows the exposure map corrected geometric sky ratio ( $r$ ) of the source to background aperture regions after overlap correction. The ratios gradually increase from  $\sim 5\%$  to  $9\%$  as the source numbers increase from the 274 to 473

<sup>22</sup> Note this is not entirely a correct statement since  $P_r$  is defined for  $S$ , the total counts in the source region, but not for  $S_C$ , the source count. The correct statement is  $S > 1.8$ .

sources. For comparison, the 473 fixed  $2''$  radius circles in a  $2.56'$  radius circle means  $r=8\%$  without considering source aperture overlap (about 100 sources) and the gaps between the CCDs. We validate our calculation of the ratios by the fact that the same aperture photometry produces the essentially null net photons in the 9–12 keV band in the combined source regions (Table 4).

Interestingly R09 quote 2% for this ratio for their 473 sources, which is a factor of four smaller than our estimate. R09 justifies their ratio based on a claim that their aperture photometry is done using the pixellated image rather than event files (Revnivtsev 2012). However, as shown in Li et al. (2004), we believe aperture photometry benefits substantially from the sub-pixel information by using event files instead of pixellated images. In addition, a few techniques have been developed and proven to reduce pixellation-induced uncertainties for aperture photometry using event files.<sup>23</sup>

Given the dominance of the background in the region, the underestimated ratios ( $r$ ) by a large factor has significant consequences. First, it mistakenly increases the resolved flux. Second, it smears the spectral diversity of sources by adding a constant term of the background spectra. Now the effect gets amplified proportionally to the number of sources since each source adds a constant background contribution into its spectrum. This generates an illusion of increase in the resolved flux as one approaches the faint side of flux where an increasingly large number of sources are added to the source list. Therefore, we believe the underestimation of the ratios ( $r$ ) contributes to the discrepancy in the X-ray luminosity distribution of the resolved GRXE. It also explains the apparent large contribution of the soft (relatively faint) sources to the resolved fraction of the 6.5–7.1 keV band in R09.

### B2 Aperture Correction for Missing Photons

When the ratio of source to background regions is  $r$ , the true net photons ( $N_C$ ) from the source is given as  $N_C = (N_S - rN_B)/(1 - X - rX) = N_N/(1 - X - rX)$ , where  $N_S$  and  $N_B$  are the total events in the source and background regions respectively, and  $X$  is the missing photon fraction due to the finite aperture size. For the fixed  $2''$  radius PSF, R09 assumed  $X$  to be 10%. This is alright in estimating the true net flux of a single point source in the field, but for calculation of the total resolved fraction in a small section of the field, there are two caveats as illustrated in Figure B1. First, the multiple source regions capture more photons than the 90% of photons enclosed by the single source aperture. Second, the large tail of the PSF (partially due to CCD read-out intervals) makes the source photons scatter even outside of the HRES region. i.e. some fraction of the missing 10% photons are outside of the HRES region altogether, which

<sup>23</sup> For instance, the exposure-corrected aperture area of a source region is calculated by multiplying the mean value of the exposure map in the source region with the geometric aperture size instead of adding up the exposure map values of the pixels inside the source region. The latter is subject to pixellation-induced errors when the aperture size is small, whereas the former is accurate even if the aperture radius is similar to a pixel size. See Kim et al. (2004) and H05.

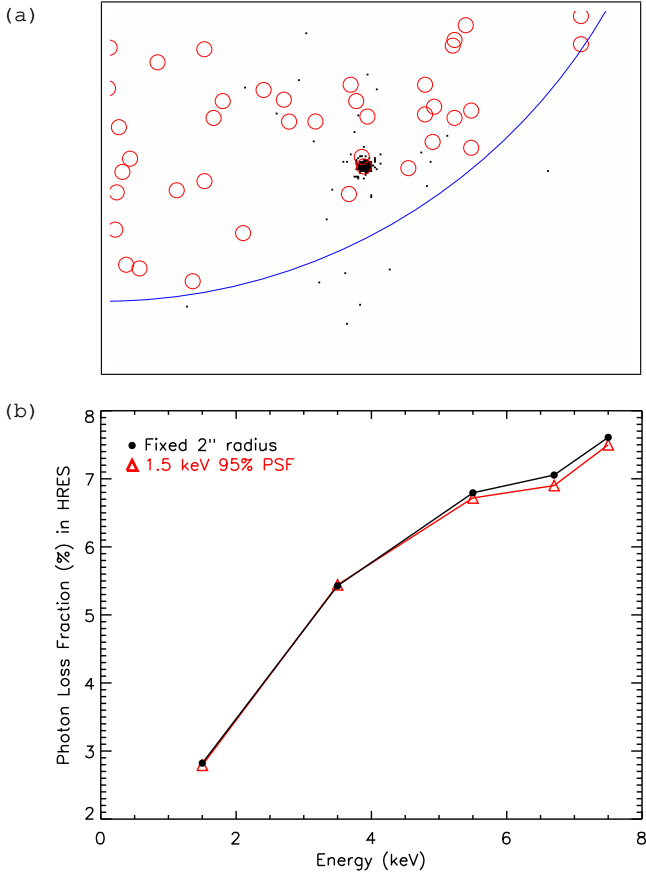


**Figure B1.** Photon loss due to finite aperture size. (a) an example of MARX simulations using 6.7 keV photons for a source near the boundary of the HRES region. Some photons outside the 2'' radius aperture of the source still fall inside of other source regions (small red circles) or outside of the HRES region altogether, which is outlined by a part of the large (blue) circle. (b) Effective photon loss fraction of the 473 sources by R09 in HRES as a function of X-ray energies, which is smaller than 10% expected for a single source in the full ACIS-I field of view (see the text). The larger variable aperture using 1.5 keV 95% PSF captures slightly more photons at high energies than the fixed 2'' radius apertures.

should not be counted for calculating the total resolved fraction in the HRES region. The latter is prominent for sources that fall near the edge of the HRES region. For the proper aperture correction, we have conducted a set of MARX simulations using various source and background regions. Figure B1b summarizes the effective photon loss fraction as a function of energies for two different aperture choices using the positions of the 473 sources detected by R09. For example, the proper correction factor  $X$  is 7.1% for the fixed 2'' radius apertures of the 473 sources in the HRES region at 6.7 keV, and 6.9% for 1.5 keV 95% PSF variable apertures. This correction factor approaches to the expected 10% as we expand the analysis region beyond HRES. Since the subsequent correction factor for the total resolved fraction is proportional to the resolved flux before the correction, so the error in the missing photon fraction can also get amplified accordingly.

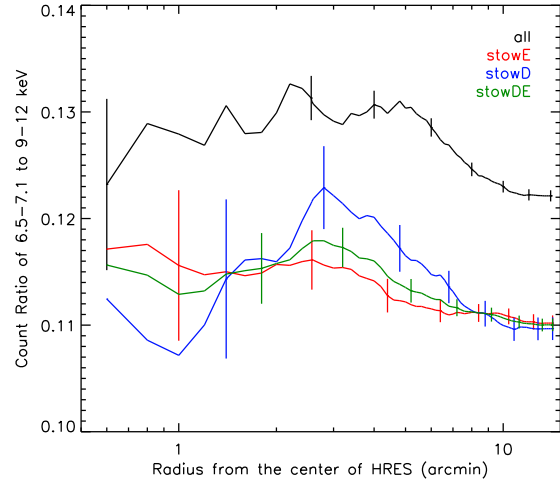


**Figure C1.** The 6.5–7.1 to 9–12 keV count ratio as a function of the enclosing radius from the center of the HRES. There is a significant fluctuation at small radii. Two stowed data sets show a large difference at small radii, but when most of the data are included, the ratios of the two data set are consistent with each other as shown in [Hicox & Markevitch \(2006\)](#).

### B3 Count Rate to Flux Conversion Factor

R09 use  $(a+bS_C^{0.8})S_C$  for the count-to-flux conversion factor, where  $S_C$  is the net source counts in 0.5–7 keV and  $a$  &  $b$  are constant ([Revnivtsev 2012](#)). This conversion solely relies on the net counts, disregarding the spectral variation of sources in the same count range, and the resulting  $S_C^{1.8}$  term artificially stretches the luminosity range. For instance, for two bright sources with  $S_C \sim 300$  and 800 in HRES that show similar spectral type under a simple powerlaw fit, it is reasonable to estimate their flux would also differ by a factor of 2.7 ( $=800/300$ ), but under the above conversion scheme by R09, their flux turns out to differ by a factor of 5. In our opinion, the conversion scheme by R09 likely misassigns the flux values of many sources, and in the resulting X-ray luminosity distribution the contribution of the faint sources appears larger than what it should be.

## APPENDIX C: ANALYSIS CAVEATS

### C1 Statistical Uncertainty of Stowed Data in HRES

The dominant contribution to the uncertainty of the total resolved fraction of the 6.5–7.1 keV flux is from the statistical uncertainty of the reprojected stowed data. In addition, there appears to be an even larger systematic uncertainty between the Period E and D data sets. How can this be since [Hicox & Markevitch \(2006\)](#) demonstrated the stowed data do not exhibit any significant variation in the flux and spectrum over the years? Figure C1 illustrates the origin, which plots the relative count ratio of the 6.5–7.1 to 9–12 keV bands as a function of the radii from the center of HRES. When most of the data in the ACIS-I chips from CCD 0 to 3 are used, which corresponds the right side of the plot (radius  $\gtrsim 8'$ ) the relative count ratio of 6.5–7.1 to 9–12 keV

do not show any significant variation between the two periods, which is consistent with [Hicox & Markevitch \(2006\)](#). But the same ratio shows large fluctuations at small radii.

In addition, for instrumental background subtraction, the stowed data are reprojected to sky according to the aspect solution of the observations as aforementioned in order to properly account for the spatial variation. Each reprojection produces different results originating from random assignment of events to the aspect solution, and each reprojected stow data shows a similar scale of fluctuation as the error bars of statistical origin in Figure C1. Note that the curves for the stow data in Figure C1 are based on the average values of 100 separate reprojections for each data set. Therefore, using a particular reprojection result may lead to a significant different outcome in the resolved fraction.

In summary, the instrumental background is sensitive to the choice of the stowed data set (D+E vs. E), VF mode cleaning, and the analysis region size (unless it is larger than 7-8' radius). Each of these can make the total resolved fraction vary by about 10% or more.

## C2 Soft vs. Hard X-ray Sources

One may argue the distinction of hard and soft X-ray sources by median energy of 2.2 keV and the subsequent association with source types like MCVs and ABs are too crude. In fact, coronally active stars exhibit spectral hardening during flares. However, a few dozen sources with some clues about their source type (e.g. Figure 3) are consistent with our division scheme, and the median energy of typical flares from coronally active stars are below 2.2 keV (e.g.  $E_{50} > 2.2$  keV means  $kT > 10$  keV for thermal plasma models with  $N_{H22} \sim 0.7$ ). Therefore, despite its arbitrary aspect, our distinction of source types with the median energy is statistically justified.

## C3 Faint vs. Bright X-ray Sources

One may claim the dominance of the relatively bright ( $\gtrsim 10^{31}$  erg s $^{-1}$ ), hard ( $E_{50} \gtrsim 2.2$  keV) X-ray sources in the resolved GRXE is because we have not resolved the flux from the faint sources although we resolved the flux of the bright sources properly. If we simply add the resolved fraction of the faint sources by R09 to the resolved fraction of our bright sources, the total resolved fraction exceeds 100%. This means there should be an error in the aperture photometry. However, it is hard to imagine any mistake in aperture photometry would channel the X-ray flux into a smaller number of sources. Errors in the analysis usually influence the results in an opposite way, smearing the outcome rather than sharpening the results. For instance, the incorrect bore-sight correction or lack thereof would smear the image, resulting more evenly spreaded events among the sources and background region. In summary, the total resolved fraction from our analysis and their dependence of the source type and luminosity strengthen the earlier conclusion that the majority of the resolved flux are from relatively bright, hard sources such as MCVs and bright AGNs.

## REFERENCES

- Brandt, W. N. et al., 2001, AJ, 122, 2810  
 Ebisawa, K. et al., 2001, Science, 293, 1633  
 Ebisawa, K. et al., 2005, ApJ, 635, 214  
 Ebisawa, K. et al., 2008, PASJ, 60, 223  
 Freeman, P.E. et al. 2002, ApJS, 138, 185  
 Gehrels, N. 1986, ApJ, 303, 336  
 Grindlay, J.E. et al., 2005, ApJ, 635, 920  
 Harrison, F., et al., 2005, Exp. Astro., 20, 131  
 Hicox, R. C. & Markevitch, M., 2006, ApJ, 645, 95  
 Hong, J, Schlegel, E. M. & Grindlay, J. E., 2004, ApJ, 614, 508 (H04)  
 Hong, J. et al., 2005, ApJ, 635, 907 (H05)  
 Hong, J. et al., 2009a, ApJ, 699, 1053 (H09a)  
 Hong, J. et al., 2009b, ApJ, 706, 223 (H09b)  
 Hong, J, et al., 2012, ApJ, 746, 165  
 Hong, J, et al., 2012, in preparation  
 Kashyap, V. et al., 2010, ApJ, 719, 900  
 Kashyap, V. et al., 2011, AAS, #228.27  
 Kaneda, H. et al., 1997, ApJ, 491, 638  
 Kim, D.-W. et al., 2004, ApJS, 150, 19 (K04).  
 Kim, E. et al., 2007, ApJ, 659, 29  
 Koyama, K. et al., 1986, PASJ, 38, 121  
 Laycock, S. et al., 2005, ApJL, 634, 53 (L05)  
 Li, J. et al., 2004, ApJ, 610, 1204  
 Markevitch, M. et al., 2000, ApJ, 541, 542 (see also [http://cxc.harvard.edu/contrib/maxim/make\\_readout\\_bg](http://cxc.harvard.edu/contrib/maxim/make_readout_bg))  
 Markevitch, M. et al., 2003, ApJ, 583, 70  
 Morihana, K. et al., 2012, Submitted to ApJ  
 Munro, M. P. et al., 2003, ApJ, 589, 225 (M03)  
 Munro, M. P. et al., 2009, ApJS, 181, 110 (M09)  
 Revnivtsev, M. et al., 2006 A&A, 452, 169  
 Revnivtsev, M. & Sazonov, S., 2007 A&A, 471, 159  
 Revnivtsev, M., et al., 2009 Nature, 458, 1142.  
 Revnivtsev, M., 2012, private communication  
 Servillat, M. et al., 2012, ApJ, 748, 32  
 van den Berg, M. et al., 2006, ApJL, 135, 647  
 van den Berg, M., Hong, J. & Grindlay, J. E., 2009, ApJ, 700, 1702 (V09)  
 van den Berg, M. et al., 2012a, ApJ, 748, 31  
 van den Berg, M. et al., 2012b, in preparation  
 Vikhlinin, A. 2002, Reducing ACIS Quienscnet Background Using Very Faint Mode (Cambridge: CXC), [http://cxc.harvard.edu/cal/Acis/Cal\\_prods/vfbkggrnd](http://cxc.harvard.edu/cal/Acis/Cal_prods/vfbkggrnd)  
 Wang, Q. D. , Gotthelf, E. V. & Lang, C. C., 2002, Nature, 415, 148  
 Wang, Q. D., 2004, ApJ, 612, 159  
 Warwick, R. S. et al., 1985, Nature, 317, 218  
 Weisskopf, M. C. et al., 2007, ApJ, 657, 1026  
 Worrall, D. M. et al., 1982, ApJ, 255, 111  
 Worrall, D. M. & Marshall, F. E., 1983, ApJ, 267, 691  
 Yamauchi, S. et al., 1996, PASJL, 48, 15  
 Yamauchi, S. & Koyama, K., 1993, ApJ, 404, 620  
 Yuasa, T., Makishima, K. & Nakazawa, K., 2012, ApJ, 753, 129  
 Zhao, P. et al. 2005, ApJS, 161, 429